Wear 540–541 (2024) 205186

Contents lists available at ScienceDirect

Wear

journal homepage: www.elsevier.com/locate/wear

Experimental and numerical investigations of sliding wear behaviour of an Fe-based alloy for PWR wear resistance applications☆

Ajit Bastola [a], Ruby McCarron [a], Philip Shipway [b], David Stewart [c], Daniele Dini [a,*]

[a] Tribology Group, Department of Mechanical Engineering, Imperial College London, South Kensington Campus, Exhibition Road, London SW7 2AZ, UK
[b] Advanced Materials Group, Faculty of Engineering, University of Nottingham, Nottingham, NG7 2RD, United Kingdom
[c] Rolls-Royce plc, Derby, UK

ARTICLE INFO

Keywords:
Sliding wear
Co- and Fe- based alloys
RR2450
Pin on disc
FEA wear prediction

ABSTRACT

The excellent wear and corrosion resistance of Co-based alloys make them desirable for tribological applications in the nuclear industry. However, neutron activation of the Co-based alloys leads to significant occupational radiation doses. An alternative Fe-based alloy called RR2450 was developed by Rolls-Royce plc to replace these alloys. This paper presents the first comprehensive study evaluating the sliding wear resistance of RR2450 alloy in representative PWR conditions. The sliding counterface of RR2450 balls was a Co-based alloy, Haynes 25 discs. Four tests were performed at temperatures up to 80 °C, and 12 tests were performed up to 200 °C. Results showed wear performance of RR2450 balls degraded at higher loads and temperatures, with temperature having a significant role. Microstructural investigation revealed voids and hard silicide phases, negatively impacting wear resistance. Nonetheless, the wear performance of RR2450 was similar to a Co-based alloy, a=Stellite 20, at nuclear reactor conditions. Two wear tests with uneven wear tracks were selected for 3D finite element analysis. The wear simulation procedure is based on Archard's wear equation and is implemented in a commercial FE package, ABAQUS. The FEA method was used to capture the wear on both surfaces, and was shown to predict nominal wear profiles. These comparisons with experiments show that the FEA results can provide representative wear profiles when wear depths and widths are asymmetrical and irregular.

1. Introduction

Pressurized water reactors (PWRs) are the most common type of reactor worldwide. Occupational radiation doses at these plants have steadily declined over the years, due to improvements in work practices and reactor design. [1,2]. However, there is still room for improvement. Metallic elements, such as cobalt and nickel, get activated under the neutron flux. The two radionuclides with the most significant impact on operational radiation exposure are Co-58 (half-life ≈ 71 days, 0.81 MeV gamma rays) and Co-60 (half-life ≈ 5.3 years, 1.1 and 1.3 MeV gamma rays). For example, these two activated isotopes account for approximately 90% of the total occupational exposure at the Sizewell B power plant in the UK. Co-58 exposure is not a significant issue after the commissioning phase due to shorter half-life [3].

The excellent wear and corrosion resistance of Co-based alloys make them desirable for tribological applications in the nuclear industry. The rolling element bearings present in control rod drive mechanism [4] are made of Co-based alloys. The Co-based alloys are also present in bearings and raceways in coolant pumps and valves. For bigger components of valves, e.g., body, stem and ball, Co-based alloys are applied to the surface by welding or thermal spraying. Wear debris produced by mechanical interactions are transported throughout the primary circuit and are deposited at various random locations. Corrosion products formed by assistance of mechanical interactions are also deposited at various locations. The materials are removed from a surface by sliding wear and wear by hard particles in combination with electrochemical corrosion mechanisms. These wear debris and corrosion products are the causes for occupational radiation exposure [5,6]

The search for a suitable replacement is an ongoing research since the early 1960s. Fe-based and Ni-based alloys are the primary focused alternatives [5–12]. The alternatives have shown a variable degree of success. However, as Bowden et al. [12] pointed out, the alternatives have not matched the elevated temperature wear resistance of commonly used Co-based alloys such as Stellite®6 (UNS R30006) and Haynes®25 (UNS R30605). Stellite 6 is a common hardfacing alloy

☆ This document is the results of the research project funded by Rolls-Royce Plc. and Engineering and Physical Sciences Research Council (EPSRC), United Kingdom through the EPSRC Centre for Doctoral Training in Nuclear Energy (EP/L015900/1) and Prof. Dini's Established Career Fellowship (EP/N025954/1).

* Corresponding author.
E-mail addresses: a.bastola17@imperial.ac.uk (A. Bastola), d.dini@imperial.ac.uk (D. Dini).

https://doi.org/10.1016/j.wear.2023.205186
Received 6 April 2023; Received in revised form 25 October 2023; Accepted 27 November 2023
Available online 7 December 2023

used in the primary circuit. Haynes 25, also known as L605 alloy, is commonly used for rolling and raceway components of rolling element bearings.

All these three families of hardfacing alloys contain some types of hard phases in a solid solution strengthened matrix. Depending on their alloying composition, typical hard phases are carbides, silicides and borides, while matrix strengtheners can be carbon, chromium, tungsten, molybdenum, niobium, and silicon.

Research on Ni-based alloys has shown lower wear resistance than Stellite and Fe-based alloys generally [11,13–16]. For instance, Deloro 50^{TM} [17] showed near zero wear loss above 200 °C but substantial wear loss at low temperatures. Meanwhile, another Ni-based alloy called Nimonic 80A [15] showed wear rate increased with the sliding speed. Inman et al. [15] state this decrease in wear rate is due to the formation of a protective "glaze layer" at the lower speeds. Ni-based alloys can be a substitute for Co-based alloys, but the operational window is severely restricted.

Another group of alloys, Fe-based alloys, have gathered greater attention [7,18–21] in recent years. NOREM 02 [22], Tristelle 5183 [21,23], Nitromaxx [24] and RR2450 [12,25] are few to name. Nitronic 60 stainless steel is one of the first alloys showing superior wear resistance in the 1970s. A typical composition (wt%) of Nitronic 60 is Fe–17Cr–8.5Ni–8Mn–4Si and 0.1C. Nitronic 60 was altered compositionally to create NOREM 02, notably by increasing carbon content (wt%) from 0.1% to 1.3%. This austenitic stainless steel developed by Electric Power Research Institute has shown mixed results. Ocken [18] state NOREM 02 matched or exceeded the Co-based alloys. However, Persson et al. [26] and Lee et al. [10] showed significant wear volume loss above 150 °C with increased friction when sliding against Stellites. Tristelle 5183 is another compositionally altered alloy from Nitronic 60 developed to improve the deformation resistance of solid solution matrix. Niobium is added, and manganese is removed, along with increasing carbon content to 2 wt%.

Meanwhile, Nitromaxx is a successor of Norem alloys that is a stainless steel supersaturated with nitrogen [24,27]. The compositions and manufacturing routes are chosen to obtain a high work-hardening rate, an ability of the material to form lubricating oxide layer on the wear surface, and low stacking fault energy that suppresses the ability of dislocations via cross slip.

The manufacturing method of the new alloys is dominated by powder metallurgy and Hot Isostatic Pressing (HIP), while the contemporary alloys, such as NOREM 02, were created from weld deposition methods. The advantages of the HIPed alloy are the presence of a very fine carbide grain structure and reduced mean free path. RR2450 is one of these new alloys patented and developed by Rolls-Royce plc [28]. It is a derivative of Tristelle 5183, a Fe-based austenetic stainless steel alloy. A typical composition (wt%) of Tristelle 5183 is Fe–21Cr–10Ni–5Si–7.5Nb–1.9C. Noticeably, RR2450 does not have any manganese with the addition of 8.5 wt% niobium and increased carbon content of 1.8 wt% compared with Nitronic 60. RR2450 contains increased silicon content of 5.5 wt%, increased niobium content and addition of 0.4 wt% Ti compared with Tristelle 5183. The presence of Niobium (stabiliser) resulted in the precipitation of coarse Nb-carbide precipitates and limited chromium-carbide precipitation. This leads to acceptable corrosion resistance in humid environments with negligible rust. However, exposure to highly oxygenated water leads to significant selective phase attack of the same Nb-carbide precipitates [29]. The addition of austenitic fcc stabilisers (C, Mn, N and Ni) with the ferritic bcc stabilisers (Cr, Mo, Si, Ti and W) doubles the strength as to common austenitic steels, with increased corrosion resistance [30]. Therefore, these changes in the elemental composition has the potential to improve strength, hardness and corrosion resistance of RR2450 in comparison to the Tristelle 5183. The advantages and disadvantages of the Fe-based alloys for the nuclear application as hardfacing alloys are summarised in Table S1 in supplementary section.

The alternatives have to demonstrate similar or superior properties when compared with the Co-based alloys in PWRs in terms of wear and corrosion. These are also expected to work in different environments, including high radiation water-wetted environment, high pressure (12 MPa) and high temperature (350 °C).

Two materials are focus of this work: Haynes 25 and RR2450. Haynes 25 is the raceway component of the sliding counterface. It is a Co-based alloy used in the bearing applications in nuclear reactors. It is a wrought alloy with single phase face-centred cubic (FCC) crystal structured alloy. Carbon content is low at <0.15 wt% to limit the impact of carbides on manufacturing processes. The FCC phase formed is metastable and is formed by solution treatment of the alloy at 1200 °C followed by rapid cooling. Due to the presence of metastable phases, carbides and other phases can precipitate after mechanical work. A heat treatment will then impart ductility to the alloy. Studies by Beattie and VerSnyder [31], Wlodek [32], Yukawa and Sato [33] and Klarstrom [34] showed presence of three carbide phases, M_6C (fcc), $M_{23}C_6$ (fcc) and M_7C_3 (hexagonal, trigonal) carbides. Deleterious intermetallics are also reported to form in Haynes 25, specially after long-term ageing. $(Co, Ni)_2(Cr,W)$ is the often stated formula for these intermetallics [32–35].

Fig. 1a shows a Back-scattered electrons (BSE) image of Haynes 25. Intermetallics and carbides on the single phase fcc matrix are distinctively visible. Large grain sizes, in excess of 100 μm are noticeable in BSE image. The large grain sizes were also observed in the optical images. The formation of slip bands made up of densely packed dislocations are expected on the grain boundaries to give the greater strength.

The counterface of Haynes 25 is RR2450 balls used in this study. RR2450 is a highly alloyed, complex Fe-based alloy designed to replace the Co-based alloys. Bowden et al. [12] characterised the microstructures of RR2450. Fig. 1b shows a BSE image of a polished RR2450 surface [20] highlighting the phases present. Duplex austenitic (FCC), γ-Fe, and ferritic (BCC), δ-Fe, phases are present in RR2450. It also contains a high fraction of carbides of the form (Nb, Ti)(C, N) and M_7C_3. High carbide fractions are due to the presence of 1.8 wt% C. A typical grain of the π-ferrosilicide phase is circled in Fig. 1b. The reported phase fraction of the combined π-ferrosilicide phase is 23%. Electron diffraction tomography performed by Bowden et al. [20] identified two types of these Fe-Cr-Ni silicide phases, silicide with and without carbon. The nano hardness measurements showed the hardness of these silicide phases (1680 HV) to be between 2 and 2.5 times higher than δ-ferrite and γ-austenite phases. Hardness of (Nb,Ti)(C,N) and M_7C_3 were 3136 HV and 2642 HV, respectively. Backscattered Electron Composition (BEC) or BSE imaging, Energy-dispersive X-ray spectroscopy (EDX or EDS) and X-ray diffraction (XRD) techniques were used to confirm these phases.

Zhao et al. [25] compared the galling performance of RR2450 alloys against similar hardfacing alloys. RR2450 retained its galling resistance up to 300 °C. However, tensile testing of RR2450 samples showed failure due to brittle fracture without any significant plastic deformation. The brittleness of the carbides contributed to the early fracture of RR2450. The presence of large silicides leads to detachment and fracture of large carbides, thus weakening the material and increasing the brittleness. Hence, comprehensive sliding wear test results are required to demonstrate the wear resistance of RR2450 alloy. Therefore, the main objective of this paper is to establish the wear resistance properties of RR2450 in reactor conditions.

Wear, which is broadly defined by ASTM G40 [36] as an "alteration of a solid surface by progressive loss or progressive displacement of material due to relative motion between that surface and a contacting substance or substances", is one of the main causes for damage and failure of components. Yet it is one of the most complex and difficult problem to determine wear. Interplay between the surrounding factors, such as load, speed and temperature; and internal factors, such as surface roughness, mechanical properties and microscopic flaws creates

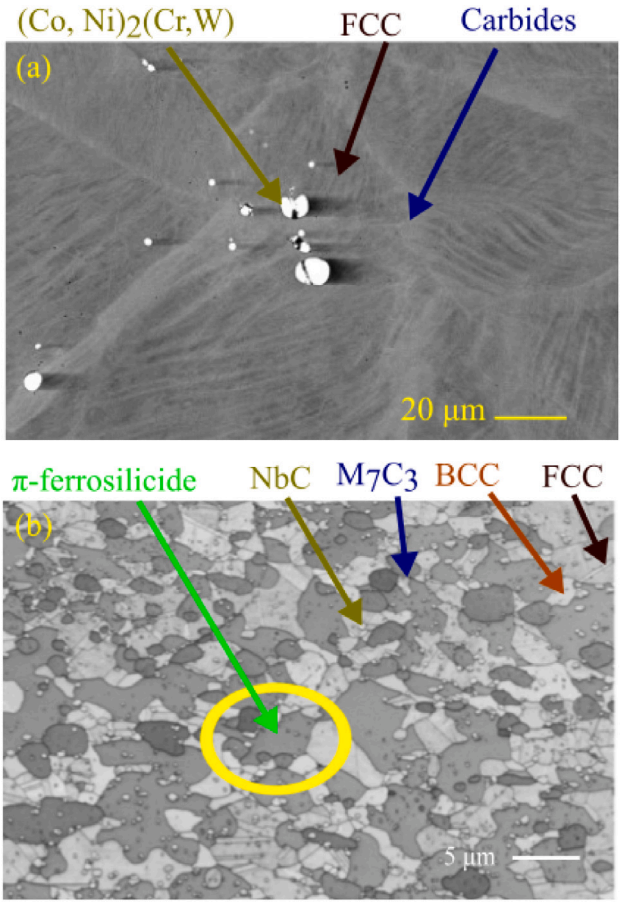

Fig. 1. BSE images of (a) polished Haynes 25 surface and (b) polished surface of RR2450.
Source: Adapted from [12].

complex challenges. Meng and Ludema [37] in 1995 showed around 300 wear models exist encompassing wide range of materials and operating conditions. The list of wear models are steadily increasing over the years.

Wear experiments are still the most reliable method to understand tribological behaviours. Pin-on-disc type wear is well established and used to determine wear and friction coefficients. The test requisites are well defined in ASTM G99 [38]. A valid alternative to experimental investigation for the study of wear is the use of models that solve non-linear contact problems using the Finite Element (FE) method to predict the evolution of the rubbing surfaces. Broadly there are two methods of wear simulation using FE. A wear model is applied at the elemental level. Archard's wear equation [39] or a modified version of this law [40] are applied at the interacting surfaces when one body is sliding against another. Another approach is to post-process the FE results with an appropriate wear model to compute the progress of wear. Once the plastic strain on the sliding surfaces exceeds a defined value, a layer of material is removed and a re-analysis of new geometries is performed. The second method is faster and require significantly less computational resources as fewer non-linear contact problems are required to be solved. Hegadekatte et al. [41] details further in these two methods.

The FEM method (FEM) developed for wear rate calculations efficiently studies very simple contact geometry [42–44], e.g. rigid cylinder on a flat surface or a rigid pin on a disc. Although these methods are adapted to solve engineering problems and use the actual geometry of the system, there are practical limitations. The analyses are slow. There are limitations on the number of degrees of freedom and the number of nodes to study the effect of local geometry with appropriate fine grid sizes. In our recent previous work, [45], a generalised three-dimensional FEM was used to determine the wear on ball and disc surfaces. For simplicity, the wear simulation procedure was based on Archard's wear law and was implemented in a commercial FE package, ABAQUS. The developed methods are appropriate for 3D surfaces, and the wear profiles are based on the accurate determination of the contact pressures.

The semi-analytical method proposed by Johansson [46], Gallego et al. [47] and Hegadekatte et al. [48] are alternative methods of computationally expensive FEM wear depth models. FEM computes wear at the nodal level, while the semi-analytical methods calculate global wear depth for each sliding increment. The global scale is applicable to relatively simpler geometry.

Unlike FEM, where contact pressures and slips are calculated, semi-analytical methods cannot predict both as these depend on the system's stiffness. These data are taken as input and are constant along the cyclic wear process. However, semi-analytical codes have been developed using misalignment of surfaces to apply contact pressures [47]. The semi-analytical wear prediction models reported in the surveyed literature were in good agreement with FEM results for the sliding and rolling wears considered.

This study is a part of broader research looking at hardfacing alloys to substitute Co-based alloys in nuclear reactor conditions. A series of sliding wear tests of RR2450 balls on Haynes 25 counterface discs are discussed in this paper. The wear performance of RR2450 is compared with the previous sliding test results of Stellites. This comparison aims to evaluate the wear performance of RR2450 as a potential Stellites replacement.

This paper has two main objectives. The first objective is to describe the test details and results of high-temperature sliding wear tests performed in conditions which are representative of the PWR environment using the two alloys selected according to the needs and motivations described above. The tests were conducted in water and ranged from room temperature to 200 °C. The second objective is to compare some of the test results with the recently developed numerical method presented in [45] and other existing semi-analytical method. The comparison is limited to wear profiles that are irregular and asymmetrical.

The paper is divided into six sections. Section 1 focused on a compilation of literature reviews on elevated-temperature wear of metallic alloys. The literature survey is limited to metallic alloys only as strict chemistry controls of nuclear power plants favour metallic components over ceramic components. The sliding wear test method and wear modelling techniques are detailed in the two subsequent sections, Sections 2 and 3. The present study's results are highlighted in Section 4. Wear performances of RR2450 is compared with a Co-based alloy's performances in Section 5. Associated experimental uncertainty and FEA model assumptions are also discussed in Section 5. Finally, the paper is concluded in Section 6.

2. Materials and test methods

2.1. Materials

The manufacturer provided nominal composition of Haynes 25 is given in Table 1 [49]. The composition of the received alloy was also confirmed with EDX microscopy. A 30% cold worked block of Haynes 25 was provided by Rolls-Royce plc with the hardness of 450 HV30. 30% cold reduction of the alloy contributed to an increased level of homogeneity of carbide precipitation during the subsequent ageing process. The block was aged at 605 °C ± 5 °C for 6 h in a furnace and air-cooled to get the desired hardness between 550 HV and 600 HV. The resultant hardness was ~570 HV30. Electronic discharge machining was then used to cut 30 mm diameter discs. The tribometer at the University of Nottingham required 10 mm thick discs. Meanwhile, the

Table 1
Chemical compositions (wt%) of two alloys.

		Fe	Co	C	Si	Cr	Mo	Ni	Mn	W	Nb	Ti
Co-alloy	Haynes 25	3.0	Bal.	0.1	0.4	20.0	1.0	10.0	1.5	15.0	–	–
Fe-alloy	RR2450	Bal.	–	1.8	5.8	21.0	–	9.0	–	–	8.5	0.50

Table 2
Load and temperature details of all the tests.

Test No.[a]	1Ia, 1Ib	1Na, 1Nb	2Ia, 2Ib	2Na, 2Nb	3Na, 3Nb	4Na, 4Nb	5Na, 5Nb	6Na, 6Nb
Normal Load [N]	10	10	10	10	10	35	35	35
Temperature [°C]	RT	RT	80	100	200	RT	100	200

[a] Letters "I" and "N" represent tests at Imperial College London and University of Nottingham respectively. Suffixes "a" and "b" are two repeats for each test conditions.

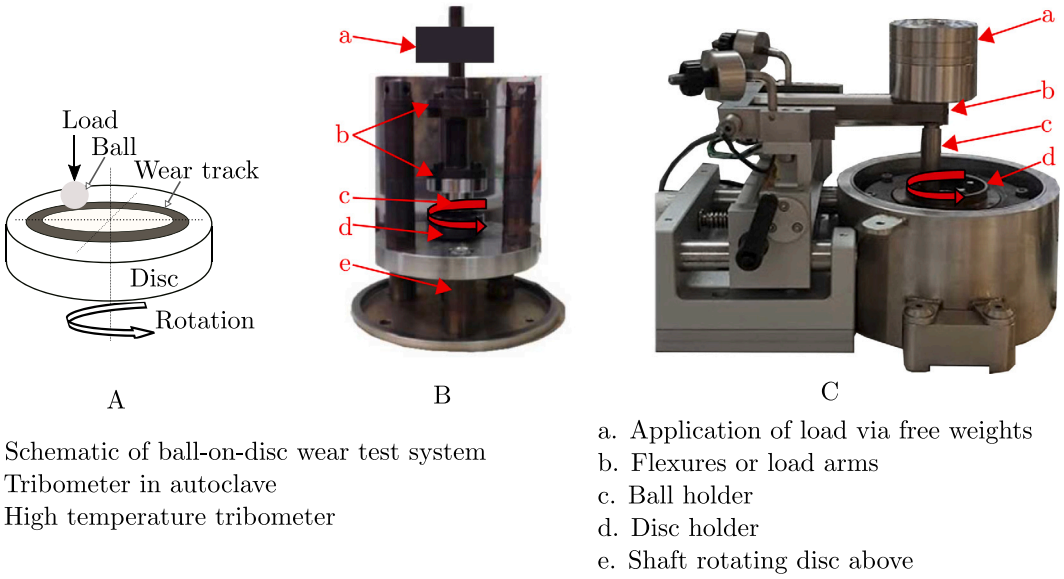

Fig. 2. Two types of tribometers used for the tests compared with ASTM G99 sketch.

Imperial College London tribometer did not require a pre-defined disc thickness. So, 5 mm discs were used at Imperial College London to make the best use of the available materials while preserving the validity of the assumptions made in the analyses.

Table 1 also lists the nominal composition of RR2450 alloy. Gas-atomised power form of RR2450 is initially produced. The powder was used to produce bars using hot iso-static pressing (HIP) at Bodycote, Chesterfield, UK. High temperature (up to 2200 °C) and high pressure (up to 300 MPa) are applied to produce a consolidated component with near-net-shape finish during HIP process [20,27,50]. The resultant hardness of the alloy was 550 HV. The bars were then machined and polished into 10 mm diameter balls by PCS Instruments, London, UK.

2.2. Wear testing

Table 2 summarises the sliding test details. Test numbers with the letter "I" are tests performed using a tribometer at Imperial College London. Test numbers with the letter "N" are tests performed at the University of Nottingham. There were 16 tests conducted in this study, and each load and temperature condition was repeated once. For example, test number 2Na is the first of the two tests performed at 100 °C with a normal load of 10 N. Test case 2Nb is a repeat of test number 2Na. This study performs the pin-on-disc type wear test as shown schematically in Fig. 2A. Fig. 2B shows the tribometer enclosed in an autoclave at the University of Nottingham. Autoclave is removed in Fig. 2B to show the primary components of the tribometer. The rotation of the disc is driven by a magnetic coupling with an external drive in this bespoke tribometer. There is a 10 mm offset between the axis of loading and the axis of rotation, resulting in a wear track diameter of 20 mm and sliding speed of 0.21 m/s at the centre of the track. Since the free weights are completely submerged in an aqueous solution, there would be some buoyancy effects. However, the buoyancy effects were negligible, with the maximum fluctuation on the contact load being <5%.

The tribometer used at Imperial College London is Anton Paar high temperature tribometer and it is shown in Fig. 2C. The load arm (annotation 'b' in Fig. 2C) can be adjusted to the required offset of 10 mm from the centre of the disc. Anton Paar tribometer is not enclosed in an autoclave, so sliding wear tests at room temperature and at 80 °C were only conducted using it. Loads on both tribometers are stabilised with a mechanism that allows free vertical movement of the load.

All the tests were run for 180 min at a constant speed of 200 rpm, so the total number of revolutions was 36 000. Once the required pressure and temperatures are achieved and stabilised, the slide wear tests were started for 36 000 cycles. In order to mimic reactor conditions, deoxygenated deionised water was used with an addition of 8.5 mg of LiOH per litre, which resulted in the solution having a pH of approximately 10.5 at room temperature. Since the concentration of boric acid fluctuates during PWR plant operation to control neutronics, boric acid was not added to the aqueous solution.

2.3. Material and surface characterisation

The hardness of the alloys was measured using Vickers hardness diamond indentor of 10 kgf and 30 kgf. Each reported hardness values

Table 3
Mechanical properties at room temperature.

	Ball	Disc
Material	RR2450	Haynes® 25
Hardness	550 HV10	570 HV30
Elastic modulus [GPa]	230	225
Poisson's ratio	0.3	0.3
Diameter [mm]	10	30
Disc thickness [mm]	–	5/10[a]
Ra surface roughness [μm]	0.29	0.13

[a] 5 mm discs were used in Imperial College London tribometer and 10 mm discs were used in University of Nottingham tribometer.

given in Table 3 is averaged from 10–15 measurements. Microstructures of bulk material and post-worn surfaces of both ball and disc samples are examined using Hitachi S-3400N SEM and JEOL 6010LA SEM. Both secondary electron (SE) and BSE imaging, along with EDX, were used in identifying the composition of any features of interest. SEM gives topographical images, while BSE gives compositional and grain contrasted images.

Phase identification was performed using an X-ray Diffraction (XRD) system. The Malvern PANalytical MPD diffractometer with monochromatic Cu-Kα (λ = 1.5406 Å) radiation was used to analyse bulk materials and wear tracks. The step size of 0.03° and the time per step of 50 s was used. A slit size of 2 mm was used to gather diffraction patterns at wear tracks and a 5 mm slit on the bulk material.

Talysurf Series 2 profilometer was used to measure the surface roughness of the samples. Roughness values were averaged from multiple measurements from two randomly selected samples. Averaged Ra = 0.29 μm and Rq = 0.41 μm for the balls. Likewise, averaged Ra = 0.13 μm and Rq = 0.17 μm for the disc surfaces. Although the averaged surface roughness of ball surfaces is higher than that of disc surfaces, the Ra values are below the threshold of 0.8 μm recommended by ASTM G99 [38] for pin-on-disc type sliding tests.

The ball and disc wear coefficients for the sliding tests are derived from Archard's wear equation and determined by the following equations:

$$k_b = \frac{V_b H_b}{S F_N}$$
$$k_d = \frac{V_d H_d}{S F_N} \quad (1)$$

where,

V_b and V_d are the total wear volumes of the ball and disc, respectively, k_b and k_d are the ball and disc coefficients of wear respectively. H_b and H_d are the ball's and disc's hardness, respectively. F_N is a normal load.

The wear volumes were measured using a 3D measuring laser microscope (LEXT OLS5000) by Olympus. The objective lens with 50x magnification with height error margin of ±50 nm was used to measure wear profiles of the discs. Since the counter face ball surfaces are curved, a lower 20x magnification lens with height error margin of ±0.5 μm was used. A typical wear scar on the ball surface is given in Fig. 3a. Wear height contour measured by the Olympus LEXT OLS5000 confocal microscope is given in Fig. 3b. Two perpendicular lines crossing at the centre of the contour plot represent lines that are used extract 2D profiles, one line is along the sliding direction and the other line is normal to the sliding direction. The curvature of the ball is removed Fig. 3b. These extracted 2D line profiles are used to compare test results with simulation results. The wear volumes of the disc wear track were measured by stitching multiple profiles. Eight profilometric measurements were made at 12 o'clock, 3 o'clock, 6 o'clock and 9 o'clock positions. Generating the entire 3D contour of the disc wear track is impractical. Thus each profilometric measurement was used to determine the cross-sectional area using Simpson's rule to integrate. The averaged cross-sectional area was multiplied by the mean circular path of the wear track to obtain the wear volume loss. The wear track profiles and optical images are given in Fig. 4 for the four locations. The direction of sliding is also annotated. The two parallel lines (red and green with arrows) displayed on each height contour plot are the locations used to extract 2D profiles.

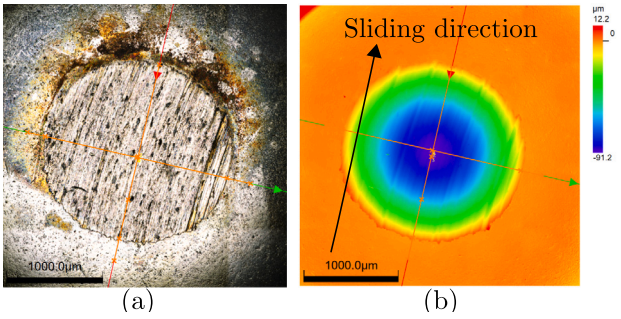

Fig. 3. Optical image (a) and wear height contour plot (b) of RR2450 ball for Case 2Na.

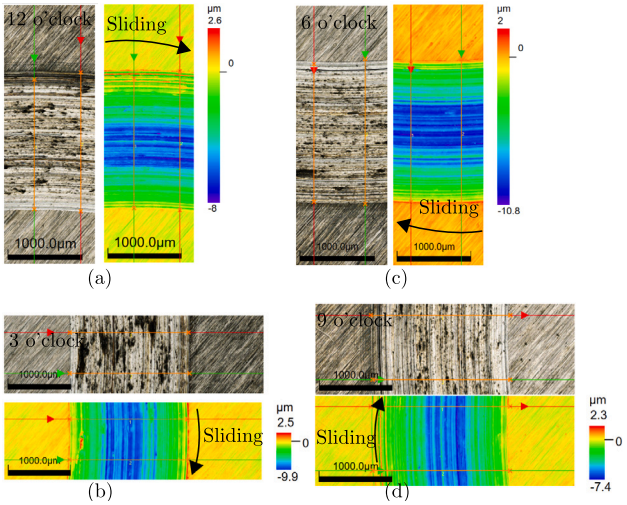

Fig. 4. Optical images of worn tracks and wear height contour plots of Haynes 25 disc for Case 2Na at 12 o'clock (a), 3 o'clock (b), 6 o'clock (c) and 9 o'clock positions. (For interpretation of the references to colour in this figure legend, the reader is referred to the web version of this article.)

3. Modelling

3.1. Semi-analytical method

The semi-analytical (SA) method proposed by Hegadekatte et al. [48] was used for initial comparison with the test results. The model uses Hertzian contact stresses and Archard's wear law to calculate the wear over a sliding increment. The inputs are geometry, elastic material properties, applied normal load, and the experimentally obtained wear coefficients. Change in wear depths and wear track widths are the outputs as a function of sliding distance. The method uses an explicit Euler method to integrate Archard's wear equation for the surface nodes and was executed in a Python console. An average contact pressure from the contact region is used to calculate the increments in wear depth, and the coefficient of friction is not explicitly included but incorporated in the wear equation as described in Hegadekatte et al. [48].

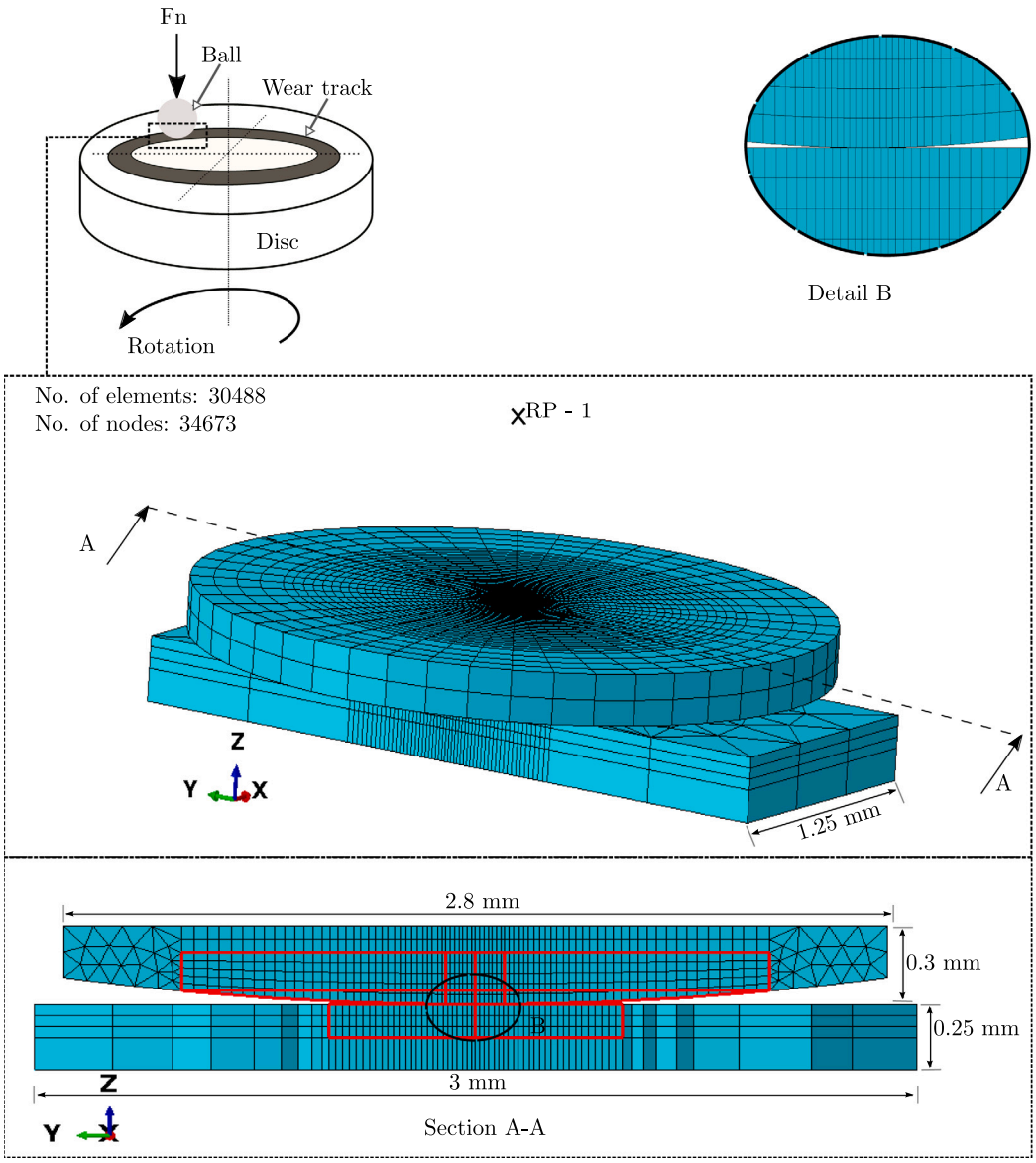

Fig. 5. FEA assembly of ball and disc for sliding wear simulations.

3.2. Numerical method

Unlike the SA method, Finite Element Analysis (FEA) uses calculated contact pressures and slip displacements to determine wear depths. Thus there is no requirement to average contact pressures over a contact area. The wear modelling technique developed to predict wear on the disc and ball counterfaces is briefly described in this section. The detailed validated method is provided in Bastola et al. [45], and only a brief overview is given here. The objective of FEA simulations in this paper is to compare the FEA predicted wear profile with tests and semi-analytical results. The study by Bastola et al. [45] used uniform wear tracks to compare the FEA models with test results. Unlike that study, this study compares these models with the two test cases with significantly uneven wear tracks.

A segment of the wear track is only modelled for the sliding wear tests, as shown in Fig. 5. The red-bordered region of Section A-A denotes Arbitrary Lagrangian–Eulerian (ALE) adaptive mesh regions. The adaptive meshing technique in ABAQUS combines the features of pure Lagrangian analysis and pure Eulerian analysis. During the Lagrangian phase, the material moves with the mesh, and during the Eulerian phase, the mesh nodes are fixed in space, and the material flows through the mesh elements. The mesh is expected to be distorted during wear, and the mesh smoothing framework implemented by ALE adaptive re-meshing is required to smoothen the mesh. Section 3.1 and Section 3.2 of [45] provide further details on the ALE adaptive meshing techniques and wear processor used in this paper. $3 \times 1.25 \times 0.25$ mm is the dimension of the disc portion modelled. The ball's horizontal length is 2.8 mm, and the vertical length is 0.3 mm at the ball's contact point. The diameter of the ball is 10 mm. The dimension selected are adequate to capture the Hertzian contact pressures. The Hertzian contact width is 0.1 mm for the highest load cases of 35 N.

8-noded linear brick (C3D8) elements are used in the contact regions for both ball and disc. C3D8R elements and six-noded wedge elements (C3D6) are used outside the ALE adaptive mesh region to reduce computation time and the total number of elements. The bottom of the disc in the X-Y plane is fully fixed. The normal load along Z-direction is applied at a reference point, RP- 1. RP-1 is kinematically-coupled to the top surface of the ball. Thus, the load is distributed on the flat top surface of the ball in the X-Y plane. The ball is reciprocating in X-direction by $\Delta x = 0.25$ mm. Since the objective here is to calculate representative contact pressure over an element length, the sliding

distance of 0.25 mm is sufficient. Fig. 5 gives other geometric and mesh details.

The automated, incremental wear simulation tool is written in FORTRAN 90 and it is based on Archard's wear equation as given in Eq. (1). Reduction of volume term in Eq. (1) to area × height results in Eq. (2). This modified equation is then implemented using ABAQUS (version 2019) and the user-defined subroutine UMESHMOTION. The assumptions and limitations of Eq. (2) are detailed in Section 3.2 of Bastola et al. [45].

$$\frac{dh}{ds} = k_D\, p(x) \tag{2}$$

where, k_D is dimensional local wear coefficient [mm^3/N mm], dh/ds is the change in wear height per unit sliding distance. $p(x)$ is the nodal contact pressure that FEA packages like ABAQUS can calculate.

The previous FEA study showed a good approximation for uniform wear tracks and widths. This study selected two sliding tests with irregular wear track widths and depths to compare test results with FE and semi-analytical methods. 10 N load case - Case 2Na, and 35 N load case - Case 5Na are selected for the two loading conditions considered.

4. Results

4.1. Materials characterisation

Backscattered Electrons (BSE) images of Haynes 25 are given in Fig. 6(a) and (b) for two levels of magnifications. Fig. 6a shows grains with darker and brighter contrasts due to the cold-rolling and annealing process. Fig. 6b shows a magnified region of Fig. 6a. The subsequent images, Fig. 6c through to Fig. 6h are EDX images qualitatively showing the elemental compositions. The low carbon content of 0.1 wt% was not detected by EDX but is present at the grain boundaries to provide carbide strengthening while maintaining the ductility. W-rich precipitations are observed in the matrix. Point spectrum at location 1 shows a W-rich region (wt%: W: 67.1, Co: 17.2, Cr: 12.3, Ni: 2.7 and traces of Mn and Fe), suggesting the W-rich intermetallic phase. Similarly, the point spectrum at location 2 also shows a W-rich region (wt%: W 69.7, Co: 17.8 and Cr: 12.6). Location 3 is a point in the Co matrix comprising of, in wt%, W: 17.0, Ni 10.1, Cr 20.9, Mn 1.9 and Fe 1.5. Precipitation of these intermetallic phases can cause embrittlement at low temperatures but are known to improve wear resistance at high temperatures [34,51].

BSE and EDX analyses were performed on a polished RR2450 alloy surface. Fig. 7a and b are for two levels of magnifications. The two circled regions in Fig. 7a are voids formed during the manufacturing process. Other features are further detailed in Fig. 7b. EDX point spectrum analyses were carried out at three distinct areas in the figure. Location 1 is a triangular Nb crystal (wt%: Nb 98.7, traces of Fe and Cr), Location 2 is Cr-rich δ phase (wt%: Cr: 58.1, Fe: 23.1, C: 13.2, Nb: 2.8, Ni: 2.0, Si: 0.9). Location 3 is austenitic matrix, comprising of, in wt%, Fe: 64.6, Cr:14.9, Ni: 13.7, Si: 6.6. EDX mapping images for the magnified images are shown in Fig. 7c through to Fig. 7h. Hard NbC are suspended in the Fe matrix. Distinct regions with silicide-rich areas are present along with Ni-rich γ phase and Fe-rich δ phase. The presence of hard silicide phases and NbC can be beneficial from a wear resistance perspective but less desirable from a toughness and corrosion resistance perspective [12].

4.2. Wear test results

The calculated volume losses for all 16 test results are given in Fig. 8(a). Volume losses for the ball, disc and combination of both losses are given for each test case. The bars represent mean values, and the error bars provide the minimum and maximum values of the ball, disc and cumulative wear. "Tribometer I" group are tests done at Imperial College London using the tribometer detailed in Fig. 2C. Likewise, "Tribometer N" are tests done within an autoclave environment at the University of Nottingham. As expected, wear volumes increased with the applied normal load. Also, total volume losses of discs were 4 times to 8 times higher than volume loss of balls for lower load and lower temperature cases, as shown in Fig. 8(b). However, at the higher load of 35 N and higher temperatures of 100 °C and 200 °C, significant wear loss is observed on the balls. Meanwhile, there was no significant change in the volume loss on the disc counterfaces under these conditions. This shows that the RR2450 balls' wear performance is degraded at higher loads and temperatures. Ball's volume losses for the Tests 3Na, 3Nb (N-10 N 200 °C) are around double when compared with Tests 2Na, 2Nb (N-10 N 100 °C) and Tests 4Na, 4Nb (N-35 N RT). The variation of disc wear volumes for all 6 tests is significantly less. This shows that temperature has a bigger role in the degradation of wear resistance properties of RR2450 balls.

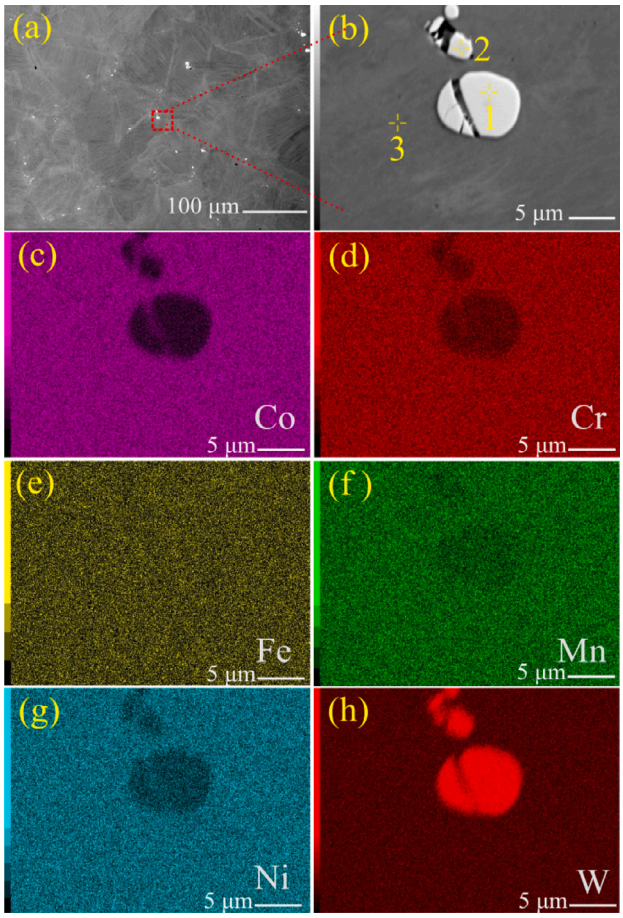

Fig. 6. (a) Low magnification BSE image of Haynes 25. (b) High magnification BSE image used for EDX elemental mapping analysis and point spectrum analysis. Co (c), Cr (d), Fe (e), Mn (f), Ni (g), W (h) were detected.

Although Fig. 8(a) shows the highest wear loss for Tests 5Na, 5Nb (N-35 N 100 °C), the error bar of the ball's volume loss shows significant variation. The ball's volume loss is almost doubled in the repeat test. Nonetheless, there is a significant increase in the ball's volume loss when compared with the Tests 4Na, 4Nb (N-35 N RT). Thus, the superior wear performance of RR2450 at lower temperatures degrades at higher temperatures of 100 °C and 200 °C.

The volume losses, hardness of the counterfaces at room temperature, total sliding distances and applied loads are used to calculate the non-dimensional wear coefficients, k_d and k_b, for the disc and ball surfaces. This is based on Archard's wear equation. Table 4 gives a detailed summary of the wear coefficients for all 16 tests. k_d and k_b wear coefficients are directly proportional to the wear volume loss.

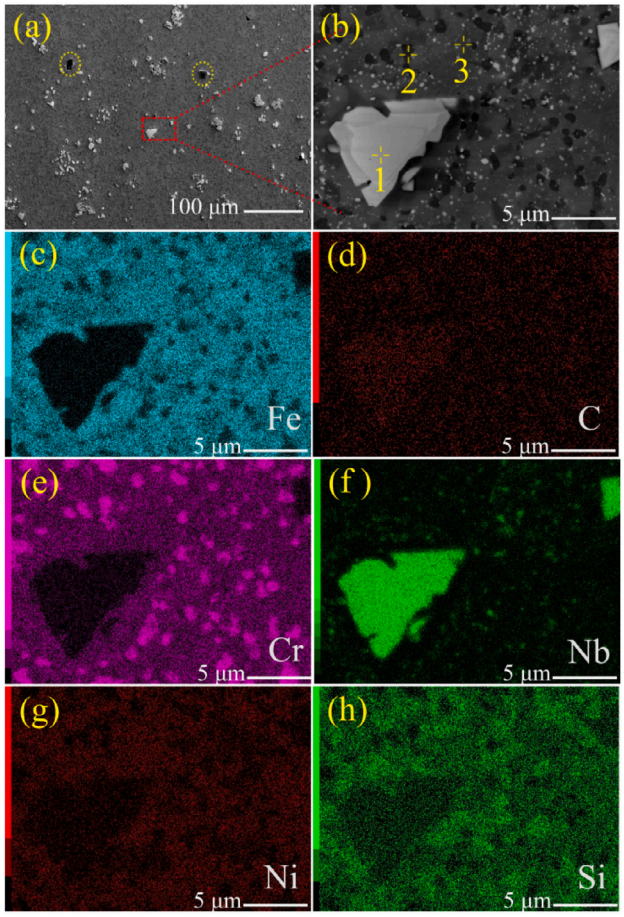

Fig. 7. (a) Low magnification BSE image of RR2450 alloy. (b) High magnification BSE image used for EDX elemental mapping analysis and point spectrum analysis. Fe (c), C (d), Cr (e), Nb (f), Ni (g) and Si (h) were detected.

Table 4
Calculated wear coefficients of disc (k_d) and ball (k_b) for all eight test conditions.

Test No.	Load [N]	Temp. [°C]	k_d	k_b
1Ia	10	RT	1.11E−04	3.82E−06
1Ib			1.97E−04	5.14E−06
1Na	10	RT	7.12E−05	6.58E−06
1Nb			1.15E−04	2.98E−06
2Ia	10	80	1.03E−04	5.07E−06
2Ib			1.56E−04	8.21E−06
2Na	10	100	1.22E−04	2.86E−05
2Nb			1.69E−04	2.73E−05
3Na	10	200	1.21E−04	8.72E−05
3Nb			1.30E−04	7.21E−05
4Na	35	RT	5.30E−05	8.17E−06
4Nb			4.61E−05	1.39E−05
5Na	35	100	9.08E−05	1.79E−04
5Nb			6.79E−05	7.50E−05
6Na	35	200	5.14E−05	1.04E−04
6Nb			6.22E−05	8.46E−05

The k_d and k_b values are used in the FEA and SA studies presented in Sections 3 and 4.4.

Fig. 8(b) also compares the wear of ball and disc surfaces at identical conditions using two tribometers. Comparing two identical test cases, Cases 1I and 1N, show insignificant changes in the total wear volume losses between two tribometers. The volume losses are within the bounds of experimental error. A comparison of the subsequent two cases, Cases 2I and 2N, shows a distinct increase in wear volumes of balls when the temperature is increased from 80 °C to 100 °C. Nonetheless, the overall volume losses are within the bounds of experimental error.

4.3. Characterisation of worn areas and surface features

Fig. 9a and b show a section of wear scars of the disc in SE and BSE modes for Test No. 4Na. Likewise, Fig. 9c and d present ball wear scars in SE and BSE modes. EDX analyses of all the wear tracks are given in the Table 5. Long-running shallow even grooves and scratches identify the sliding direction. The smooth area of the track implies that the material was ploughed smoothly from the disc surface. Features 1 and 2 in Fig. 9a and b show fragments of wear debris. This was seen at many other locations in the track for both repeats. EDX analysis of these features revealed a composition similar to Haynes 25. This indicated that some Haynes 25 debris remained in contact as the sliding interaction progressed, referred to in the literature as active wear debris [52]. Some literature [11,53] suggested that sintering due to high flash temperature and high contact pressure can cause wear debris adhesion. However, confirming that this happened in these interactions was not possible.

The border of the ball wear scar is feature 1 in Fig. 9c and d, has a smooth appearance. EDX analysis revealed the presence of Co on the wear scar surface, implying that material transferred from the disc to the ball surface. Fragments of debris and significant topographical damage were not observed as commonly as on the disc track surface. Features indicating adhesion of wear debris are observed frequently across the wear track, an example of which is highlighted in Feature 1 in Fig. 10a and b. An elevated wt% of iron within this feature was observed and it confirmed the presence of debris from the RR2450 ball in this location, see Table 5. Elevated wt% of Fe was also observed at other similar features across the track produced at this test condition. It suggests that the non-uniformity observed across the track surface produced at 100 °C may be due to adhesion of wear debris rather than uneven material removal. As the track became less uniform in appearance, the wear volume measured for the disc track decreased. The wear debris that adhered to the surface in the interaction may have protected the disc from further wear, which agrees with the discussion presented by Stott [54] and Inman and Datta [55].

The damage to the ball surface produced at 100 °C was more severe than at room temperature. The scar also had a more grooved appearance corresponding to the increase in topographical damage observed on the disc surface tested at this condition. The feature highlighted in Fig. 10c and d had slightly elevated levels of cobalt, but relative to the average scar spectrum, it was not significant.

At the experimental temperature of 200 °C under a normal load of 35 N, the topographical non-uniformity on the disc track observed was more severe than at the lower temperature conditions, see Fig. 11a and b. Features showing plastic deformation with entrapped wear debris are visible. EDX analysis of the features indicated that this contained elevated levels of iron, indicating the debris transfer. The formation of a protective oxide glaze at temperatures above 150 °C was discussed by Pauschitz et al. [11]. It was noted that these glazes might form from wear particles that were mechanically broken down into fine particles by ‘communition’ and tended to concentrate around features such as grooves in the wear track [11]. This description has similarities to what is observed in Fig. 11a and b suggesting that a protective oxide glaze may have formed. The literature [11,56] suggests that wear will transition to a mild wear regime in the presence of these glazes. This also agrees with the reduction in wear volume measured on the disc track in the 200 °C temperature condition under a load of 35 N. The polished appearance of the ball scar is once again observed, see Fig. 11c and d, agreeing with the observed increase in wear volume.

Generally, the significant variation in the uniformity of the scar in the disc wear track as a function of operating conditions is linked to

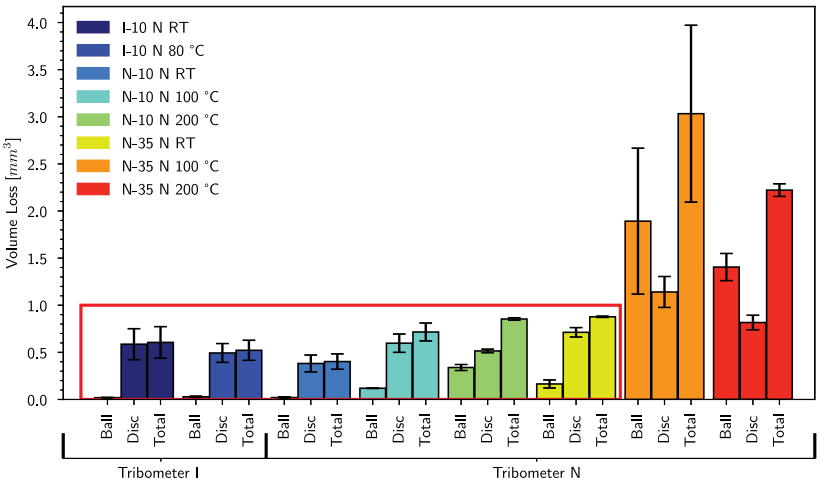

(a) Volume loss from 8 test conditions

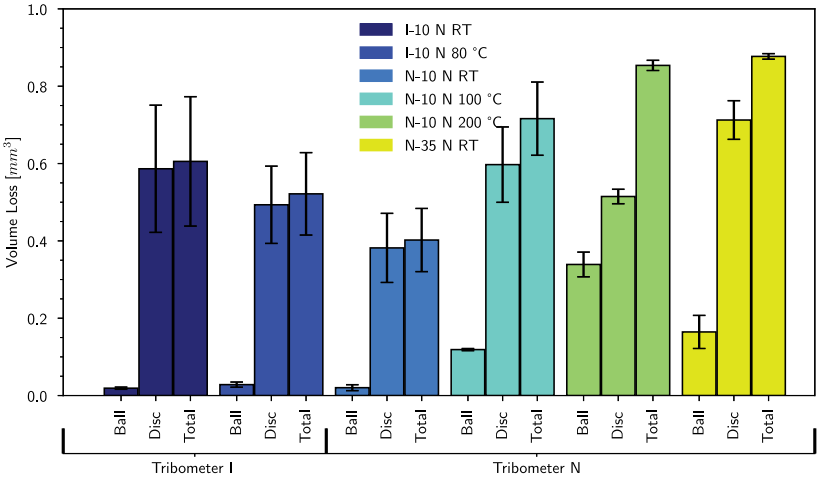

(b) Detailed volume losses below 1.0 mm^3 for 6 test conditions

Fig. 8. Summary of volume loss from all 16 tests.

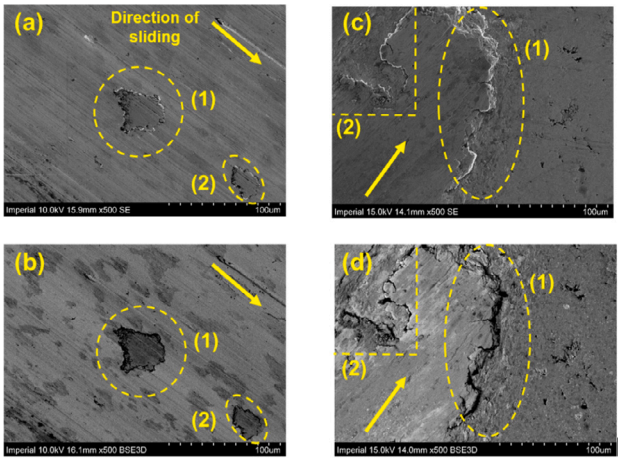

Fig. 9. (a) SE and (b) BSE of an area within disc wear track, and (c) SE and BSE (d) of an area in ball wear scar from Test No. 4Na (N-35 N RT).

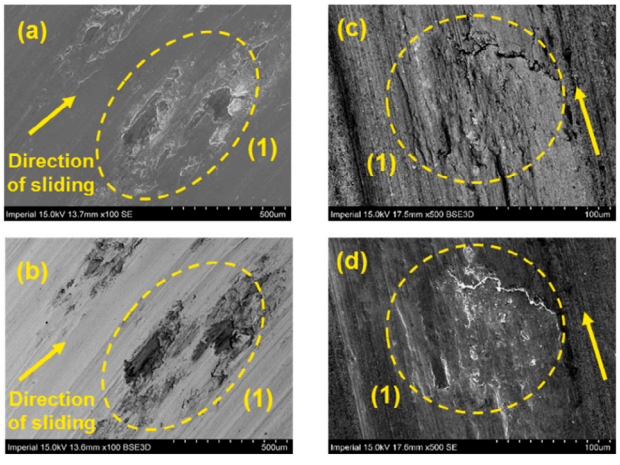

Fig. 10. (a) SE and (b) BSE of an area within disc wear track, and (c) SE and BSE (d) of an area in ball wear scar from Test No. 5Na (N-35 N 100 °C).

Table 5
EDX elemental compositional analysis of wear track at the regions shown in Figs. 9, 10 and 11.

Case No. (Test details)		Figure	Feature	Elements (wt%)										
				C	O	Si	Cr	Mn	Fe	Co	Ni	Nb	W	Total
4Na (35 N @ 20 °C)	Disc	9(a) and (b)	Average track spectrum	4	6	–	18	2	3	44	9	–	14	100
			Smooth track	3	2	–	19	2	2	47	9	–	16	100
			Feature 1 and 2: fragments of wear debris	5	11	<1	16	1	9	37	9	–	11	100
			Dispersion	8	28	<1	16	1	6	28	6	–	7	100
	Ball	9(c) and (d)	Average scar spectrum	8	10	4	18	<1	32	13	9	4	1	100
			Undamaged surface	7	–	6	22	–	47	–	9	8	–	100
			Smooth scar	5	7	3	18	<1	38	10	9	7	2	100
			Feature 1: significant topographical damage at scar border	3	17	2	16	<1	18	27	9	2	5	100
			Feature 2: topographical damage	–	14	4	17	–	40	11	9	4	1	100
5Na (35 N @ 100 °C)	Disc	10(a) and (b)	Average track spectrum	2	3	–	19	1	8	42	9	–	15	100
			Smooth track	2	<1	–	20	2	2	48	9	–	16	100
			Feature 1: topographical damage within wear track/debris	4	11	3	18	<1	31	15	9	4	4	100
	Ball	10(c) and (d)	Average scar spectrum	6	6	5	21	–	44	2	9	7	–	100
			Smooth scar	6	6	5	22	–	45	–	8	8	–	100
			Topographical damage with some adhesion of debris	11	11	3	16	–	36	9	8	4	2	100
6Na (35 N @ 200 °C)	Disc	11(a) and (b)	Average track spectrum	4	6	–	18	2	6	41	9	–	14	100
			Smooth track	2	2	–	19	2	3	47	9	–	16	100
			Topographical damage	3	17	2	17	1	18	24	8	2	8	100
			Fine, powder like debris	4	10	–	17	2	9	38	8	–	12	100
	Ball	11(c) and (d)	Average scar spectrum	–	12	4	21	<1	39	9	9	4	2	100
			Smooth scar	4	9	4	20	<1	43	5	9	5	–	100
			Topographical damage at border	4	7	4	<1	20	1	45	5	9	4	100

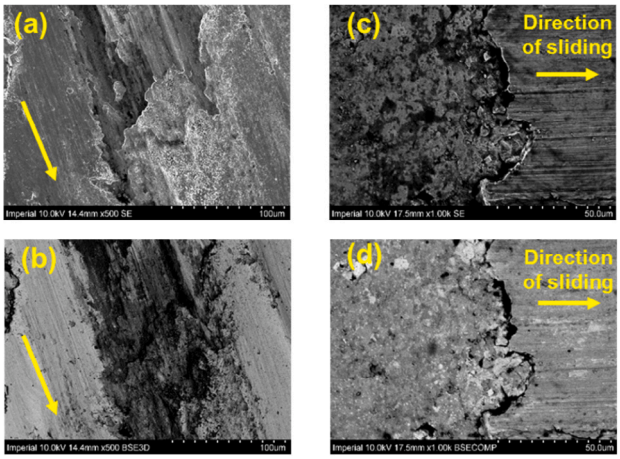

Fig. 11. (a) SE and (b) BSE of an area within disc wear track, and (c) SE and BSE (d) of an area in ball wear scar from Test No. 6Na (N-35 N 200 °C).

the changes in mechanisms due to the severity of the applied load and running temperature, with increased non-uniformity coinciding with increase of adhesive wear and formation of significant wear debris and material transfer between the mating surfaces. Conversely, the appearance of protective oxide glazes may result in a more uniform appearance of the wear track.

Phase identification of both alloys was carried out using the X-ray diffraction technique for the Test Case 6Na. The background intensity counts are removed, and the patterns are normalised to the peak of maximum intensity on each diffractogram. The resultant XRD patterns are given in Fig. 12 for Haynes 25 and Fig. 13 for RR2450 alloy. The X-ray patterns typically originate within ~20 μm depth, but the majority of diffractions originate from the top few microns. Thus, the XRD captures the present phases on the top few microns. A comparison of the disc's wear track with an area away for the wear track is made in Fig. 12 for Haynes 25 alloy. The XRD patterns were compared with the XRD patterns of Co-Cr-Fe-Mn-Ni alloy, ICDD: 04-022-8761 and Haynes 25 XRD patterns by García Fresnillo et al. [35] and Luo et al. [57] at room temperature. Patterns show peak intensity at $2\theta = 43.4°$ and is identified as γ-Co_7W_6 rhombohedral structure. Peaks at $2\theta = 50.8°$ and 74.8° are also of γ phase. Another peak at 90.8° and a smaller peak at 95.9° are Co_3W and W precipitates, respectively. Comparing the XRD patterns at the wear track against an area away from the wear track shows identical peak locations with slightly different peak intensities. There are reductions in all peak intensities for γ and Co_3W phases, but the W precipitates intensity has not changed. This can result in a smoother wear track with increased contact area and reduced contact pressures, which in turn reduces the wear volume. Carbide precipitations were not detected in the selected regions.

XRD patterns of RR2450 alloy given in Fig. 13 were compared with results from Bowden et al. [12]. XRD peaks show the presence of five phases. The primary phases are duplex austenite (γ) and ferrite (δ) microstructure. There is also a significant presence of silicide phase, approximately ~25%. The high carbon content of 1.8 wt% resulted in a high fraction of carbides of the form (Nb,Ti)CN and M_7C_3, where M is a mixture of Cr and Fe. A comparison of XRD patterns of the unworn area with the wear track shows a few silicide peaks missing. It confirms the removal of these hard silicide phases during sliding as wear debris.

4.4. Comparison of wear test results with FEA and SA method

As mentioned in Section 3.2, the objective of comparing FEA results with the test results is to check the validity of the developed FEA method when wear track widths and depths are uneven. The two selected cases, Cases 2Na and 5Na, have the highest wear track width and depth variance.

The dimensionless wear coefficients given in Table 4 are converted to dimensional wear coefficients (k_Ds). The k_Ds for the ball and disc are then used in the FEA and SA models. After solving the contact mechanics equations, the wear depths are calculated using Eq. (2). The corresponding contact width ($2a$) are measured from the deformed surfaces of the FEA models.

A summary of the maximum wear heights (h) and the widths are given in the 'Test' columns of Table 6. ALE domain required to capture

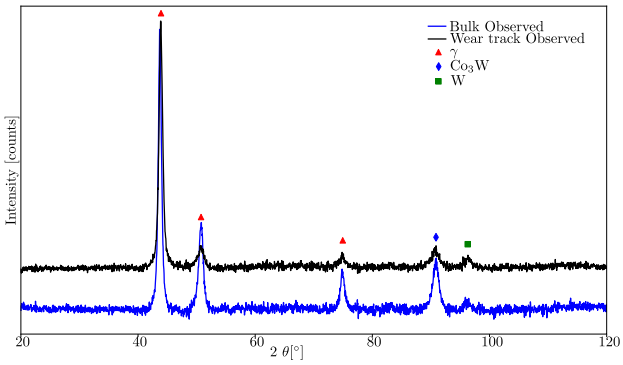

Fig. 12. XRD patterns of unworn region and wear track region of Haynes 25.

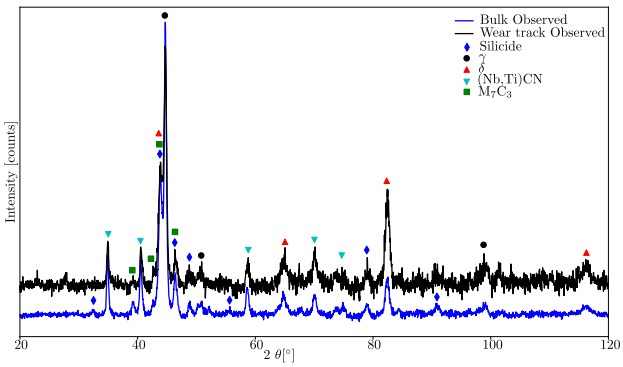

Fig. 13. XRD patterns of unworn region and wear track region of RR2450 alloy.

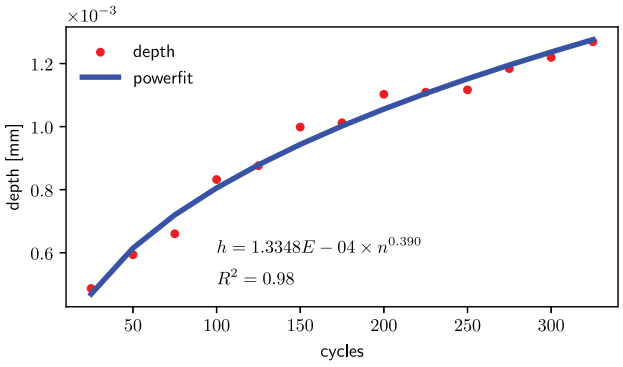

(a) Disc wear depth curve fitting

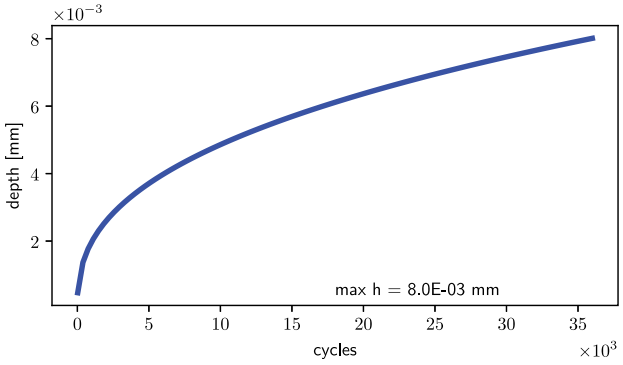

(b) Disc wear curve extrapolated to total number of cycles

Fig. 14. Case 2Na — Prediction of disc wear depth.

h ~ 0.43 mm and 2a ~ 4.00 mm would be significantly bigger than the present domains. The present simulation time of around 22 h will increase enormously. So, only a limited number of wear cycles are considered to get the trend of wear profile changes. FEA determined h and 2a parameters are then extrapolated to the required number of sliding cycles. The extrapolation method is detailed in Bastola et al. [45], and a brief overview is given here.

The wear step size of 25 was used for the 2Na test case. So the FEA predicts wear profiles for the first 325 sliding cycles. The predicted wear depths of disc and ball are given in Figs 14(a) and 15(a). Selecting suitable wear step sizes is iterative. The method by McColl et al. [58] is used to determine a stable step size. When the step sizes are above a certain threshold step size, instability occurs and contact formulations do not converge. Once the critical threshold step size is determined, the corresponding critical wear depth per sliding step, Δh_{crit}, is derived. Δh_{crit} for one load case is calculated and then the stable step size for other load case simulations are determined, using trial and error, by comparing the corresponding initial Δh to Δh_{crit}.

The least-square curve-fitting is used to fit the FEA results to a power curve in the form of $h = An^B$, where h is the wear height or wear depth, A and B are constants, and n is the cycle number. h as a function of n satisfies a power curve when the wear rate is linear and mild. Due to wear progression, the contact area increases as the material loss occurs except in non-conforming contacts. This leads to a decrease in the bearing pressure. Since wear depth is directly proportional to the bearing pressure, the change in wear depth is also decreasing. It can be seen from Fig. 14(a) that the slope of the wear depth curve is steadily decreasing with the increased number of cycles, showing a sub-linear variation. This "running-in" behaviour, along with the linear wear in the steady state, can be captured by a power-law curve. See Section 4.2 of Bastola et al. [45] for the studies performed in our previous contribution to demonstrate this. The predicted $h = An^B$ equations along with R-squared value are given in Figs 14(a) and 15(a). Here R^2 is >0.98. The extrapolated results to 36 000 cycles are then given in Figs 14(b) and 15(b).

Wear widths were also calculated using the same curve fitting method and extrapolation. Fig. 16(a) shows the calculated width for the first 325 cycles. Unlike the gradual increment in the wear depth of the ball, the wear width in this case is increasing in steps. This is because of the limited number of elements used across the sliding direction to reduce simulation time to a limited number (12 to 24) of CPU hours. The calculated width is based on the displacement of the nodes on the ball across the sliding direction. Every FEA wear step does not lead to a change in the wear width. Wear width is the total length of the elements whose vertical displacement is not equal to 0. Once the edges of the wear width fall beyond the elements that were in contact, the contact width is increased by the length of the elements. The equation derived from the power curve fitting is then extrapolated for the 36 000 cycles. The extrapolated plot is shown in Figure S1b in the Supplementary section. The FEA predicted results are then compared with the test results in Fig. 17(a) for the ball and Fig. 17(b) for the disc.

Two profiles at 12'clock and 6 o'clock positions are compared with the FEA result in Fig. 17(b). The other two profiles, at 3 and 9 o'clock positions, are also compared for completeness in the Supplementary section, Figure S2. Variations in wear profiles were observed at all four locations. Wear depths and widths were the highest at 6 o'clock positions and the lowest at 9 o'clock positions. The average wear depth from 8 measurements of disc wear depth was 7.07 ± 0.49 μm, while FEA predicted wear depth at 8.03 mm. The track width predicted by FEA was 1854.44 μm, while measured track widths range from 1887.38 μm to 1987.14 μm. The detailed profile measurements are given in Table S2 of the Supplementary section.

The ball worn profile is across the contact width and it shows asymmetric wear on the ball surface. The ball's form is removed here by

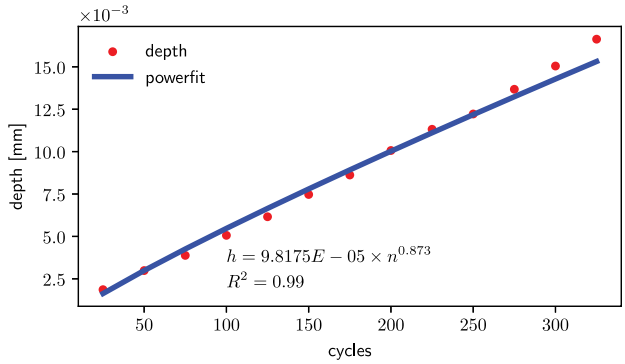

(a) Ball wear depth curve fitting

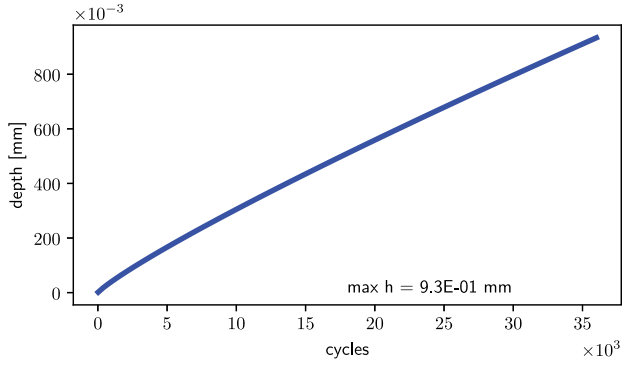

(b) Ball wear depth curve extrapolated to total number of cycles

Fig. 15. Case 2Na — Prediction of ball wear depth.

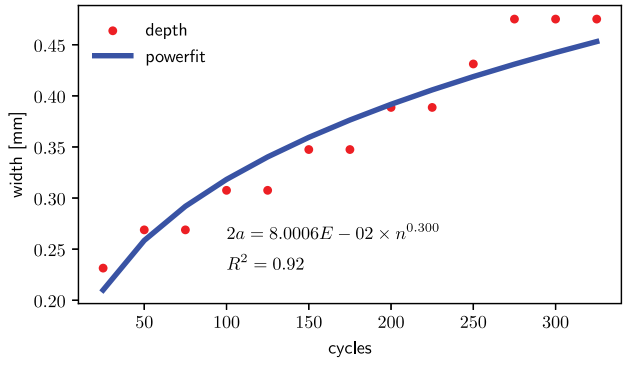

(a) Disc wear width curve fitting

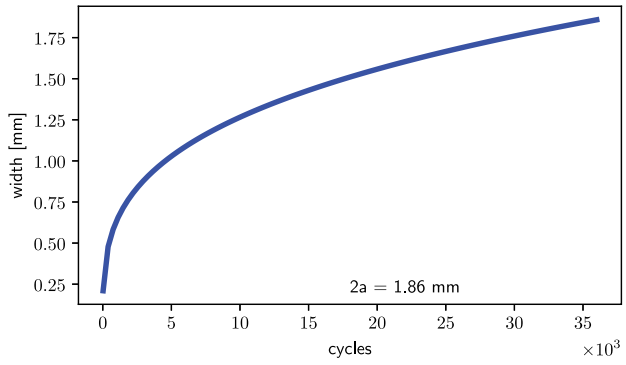

(b) Disc wear depth curve extrapolated to total number of cycles

Fig. 16. Case 2Na — Prediction of disc wear width.

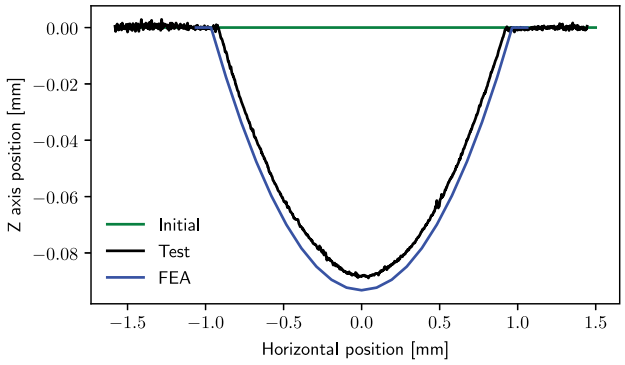

(a) Wear profile of ball in comparison with the test (form removed)

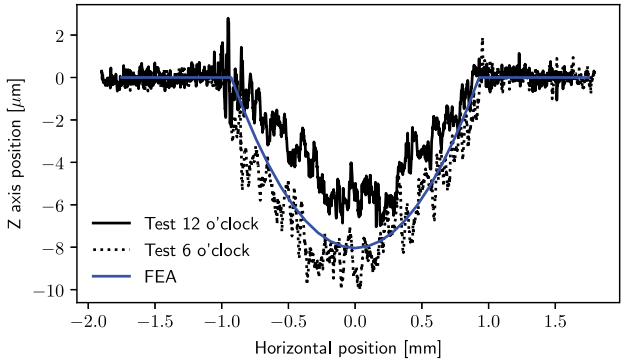

(b) Wear profile of disc in comparison with the test

Fig. 17. Case 2Na — FEA results comparison with the test results.

linearising the profile with the ball's radius of 10 mm. Removal of the form allows precise measurement of wear depths, but asymmetric wear shape on the ball wear scar is lost. All three profiles in Fig. 17(a) are profiles with the form removed. Without removal of the form, wear is the highest at the frontal region of the ball along the sliding direction. Meanwhile, the wear height is the lowest at the rear region of the ball along the sliding direction. The ball's wear scar is elliptical. The detailed measurements are given in Table S3 of the Supplementary information section. The FEA does not capture this asymmetric behaviour due to the smoothening function applied at the first increments of the sliding steps. "Test" profile corresponds to a profile normal to the sliding direction. The FEA overpredicted the wear track depth by 4.9%, and the FEA width is within error margins of test results.

Case 5Na disc wear is significantly non-uniform across the track. The wear depth ranges from 4.33 μm to 19.03 μm (mean = 11.62 ± 1.90 μm) and the disc wear track widths ranges from 3748.61 μm to 4054.39 μm (mean = 3915.54 ± 40.16). The test results are detailed in Table S4. This almost five-fold variation in wear depth, due to localised effects linked to material transfer and localised adhesion and formation and evolution of wear debris, cannot be captured with the current FEA method. Instead, the mean wear depths and heights are compared with the FEA results. Comparable wear depth of 8.65 μm and width of 3.86 mm were obtained from FEA. The curve fitting method to extrapolate wear width resulted in unrealistic disc wear track width, with R^2 = 0.82 indicating high variability. Bias mesh was used to reduce the number of elements in the ALE region of the disc. Element widths progressively increased further away from the initial contact region. Disc element width is 15 μm at the initial contact point and 30 μm at 0.5 mm in normal to sliding direction. A denser mesh was used in the ball. Element widths ranged from 15 μm at the initial contact region and 20 μm further afield. This lead to a more precise

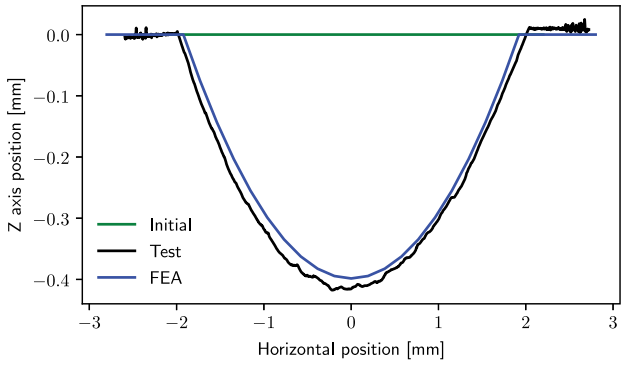

(a) Wear profile of ball in comparison with the test (form removed)

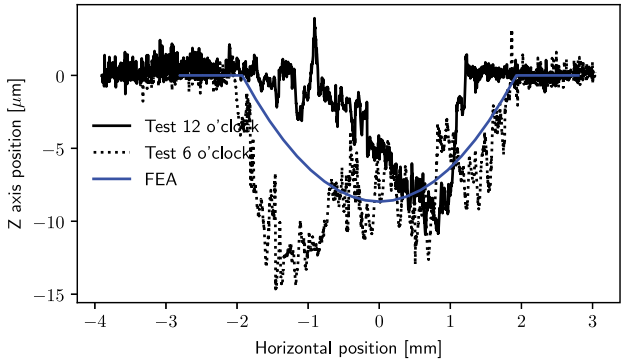

Fig. 18. Case 5Na — FEA results comparison with the test results.

wear track width capture on the ball surfaces than on the disc surfaces. A typical variation on the wear track widths of ball and disc are insignificant. Thus, the wear track width of the ball surface was selected for comparison with the test results. The curve fitting and extrapolation plots for Case 5Na are given in the supplementary information section. Figures S3a and S3b are for the ball wear depth, and Figures S4a and S4b are for disc wear depth prediction. Figures S5a and S5b show prediction of wear scar width of ball.

The wear step size of 3 was used for the 5Na case. The resultant ball wear profile is compared with the test result in Fig. 18(a). FEA predicted wear scar depth was 398.46 μm and the measured depth from test was 433.73 ± 0.92 μm. Likewise, the wear profiles from the FEA are compared with test results at 12 o'clock and 6 o'clock positions in Fig. 18(b). The remaining 3 o'clock and 9 o'clock positions are plotted in Figure S6 of the Supplementary section. Wear profiles at 12 o'clock and 6 o'clock positions maintain parabolic profiles, while the profiles at 3 o'clock and 9 o'clock positions are asymmetric. FEA predicted profiles matched well with the profile at 6 o'clock positions. A detailed comparison summary is given in Table 6.

Test results were also compared with semi-analytical results. The SA method predicted nominal wear depths and widths. Similar wear depths and widths as those predicted by FEA are observed for both cases. Due to the significant variation in wear profiles of the disc surfaces, the FEA and SA predicted results are within the measured dimensions but it is difficult to preform direct comparisons of the worn profiles. Nonetheless, a comparison with mean wear heights and depths were carried out for illustrative purpose. The maximum deviation for both FEA cases was 11%, including the error margin for the disc wear track height. Unlike the disc wear tracks, the ball wear profiles do not have significant variations and are predicted better by both FEA and SA methods. The maximum deviations were for Case 5Na. The results obtained using FEA underpredicted ball wear height by 8% while the SA method underpredicted ball wear width by 4%.

These comparisons show FEA results should be used cautiously when wear depths and widths are asymmetrical and irregular. The method, as implemented in the current framework, does not allow to explicitly consider the local variations at the contact interfaces, which are responsible for the inhomogeneous evolution of the worn surfaces. The FEA predicted wear profiles are therefore only representative of actual profiles, and the complex phenomena resulting in irregular wear tracks are not captured.

5. Discussions

The first objective of this paper is to detail the wear resistance properties of RR2450 alloy against the Haynes 25 counterface. A previous study by McCarron et al. [59] compared the wear resistance of Stellite 20 balls against Haynes 25 disc counterfaces. The same tribometers were used for this study. Stellite 20 is a similar Co-based alloy to Stellite 6, a common hardfacing alloy used in the primary circuit of PWRs. Stellite 20 has 33 wt% Cr, 16 wt% W and high carbon content of 2.45 wt%. Hardness is also higher than RR2450 at 56–63 HRC (612–775 HV). Wear volumes in this paper were compared with wear volumes given in McCarron et al. [59]. The comparison for each of the test cases are given in Table 7. Since the wear loss volumes reported for the ball's wear scar are calculated using the LEXT OLS5000 confocal microscope, so no errors are reported. The errors reported for the disc wear volume loss are statistical errors based on the standard deviation of the measurements. Meanwhile, McCarron et al. [59] used a while light interferometer to measure wear volumes. It showed RR2450 ball performed better at room temperature under 10 N load than the Stellite 20 ball. In contrast, with the increased temperature to 100 °C, the wear resistance of Stellite 20 was superior. The comparison also showed that the combined wear volume of the ball and disc was greater for the Stellite 20-Haynes 25 contact pair in each temperature condition apart from one experimental outlier at 100 °C.

Both sets of experimental results indicate that RR2450 demonstrates better wear resistance to Stellite 20, particularly at the higher load cases of 35 N. With an increase in normal load to 35 N, an increase in wear resistance of RR2450 compared to Stellite 20 was observed. Wear volume measured on the Haynes 25 discs was also notably lower on the RR2450-Haynes 25 experiments than on the Stellite 20-Haynes 25 experiments. In both cases, under a load of 35 N, the wear of Haynes 25 decreased slightly with an increase in temperature. There was no noteworthy impact on the wear performance of Haynes 25 in either loading condition, omitting results considered experimental outliers.

The Stellite 20 ball wear volumes increased with high temperatures. For instance, Table 7 shows wear volumes of Stellite 20 balls are 2–4 times higher than that of RR2450 balls. This increase in wear loss of Stellites is attributed to tribocorrosion [60,61]. Tribocorrosion is a process that combines wear and corrosion. It occurs when mechanical interactions and electrochemical processes cause the counterfaces to corrode faster than they would under static conditions. The corrosion also enhances the wear process [62]. Ratia et al. [61] proposed rate of oxidation of Stellite alloys increases with increased temperatures. This oxide layer is then repeatedly worn away by mechanical forces, which leads to more wear at higher temperatures. Meanwhile, the sliding wear tests of RR2450 balls at high temperature showed mass loss increase was not as steep as that of Stellite 20. It was not possible to decouple the wear and corrosion contribution to the mass loss of RR2450 with the current tribometer setup. An electrochemical measurement system is required to be integrated with the tribometer to quantify the contribution of tribocorrosion. It is a part of the future work.

The wear surface characterisation detailed in Section 4.3 showed polished appearance of the ball scar in the 200 °C temperature condition under a load of 35 N. Unlike Stellite 20, the effect of tribocorrosion is not pronounced for RR2450 balls. The wear volumes of balls at 200 °C are similar to that at 100 °C. The presence of protective oxide

Table 6
Comparison of the sliding wear tests results with FEA and semi-analytical methods.

Test number	2Na			5Na		
	Test	FEA	SA	Test	FEA	SA
Disc: h [μm]	7.07 ± 0.49	8.03	7.11	11.62 ± 1.90	8.65	8.63
Disc: 2a [μm]	1895.74 ± 19.66	1858.44	1870.42	3915.54 ± 40.16	3856.64[a]	4002.34
Ball: h [μm]	88.51 ± 0.40	93.25	88.20	433.73 ± 0.92	398.46	417.86
Ball: 2a [μm]	1903.38 ± 39.27	1929.43	1870.41	4033.06 ± 11.78	3856.64	4002.34

[a] R^2 less than 0.85 so ignored for extrapolation.
Taken same as ball wear track width for comparison.

Table 7
Comparison of the test results from this study with the previous study [59] using tribometer of UoN.

Load [N]	Temp. [°C]	RR2450 vs. Haynes 25			Stellite 20 vs. Haynes 25		
		Test name	Wear volumes [mm^3]		Test name	Wear volumes [mm^3]	
			Ball	Disc		Ball	Disc
10	RT	1Na	0.028	0.292 ± 0.033	1Na-St	<0.01 ± –	0.124 ± 0.053
10	RT	1Nb	0.013	0.471 ± 0.024	1Nb-St	0.056 ± 0.001	0.290 ± 0.038
10	100	2Na	0.122	0.500 ± 0.057	2Na-St	0.004 ± 0.001	0.280 ± 0.041
10	100	2Nb	0.116	0.695 ± 0.090	2Nb-St	0.095 ± 0.001	0.310 ± 0.065
10	200	3Na	0.371	0.496 ± 0.054	3Na-St	0.818 ± 0.018	0.834 ± 0.213
10	200	3Nb	0.307	0.534 ± 0.046	3Nb-St	0.947 ± 0.031	0.625 ± 0.261
35	RT	4Na	0.122	0.763 ± 0.092	4Na-St	0.125 ± 0.043	3.120 ± 0.487
35	RT	4Nb	0.207	0.663 ± 0.039	4Nb-St	0.281 ± 0.030	1.810 ± 0.203
35	100	5Na	2.666	1.305 ± 0.289	5Na-St	2.020 ± 0.195	2.110 ± 0.324
35	100	5Nb	1.118	0.976 ± 0.089	5Nb-St	4.100 ± 1.200	3.050 ± 0.645
35	200	6Na	1.549	0.739 ± 0.053	6Na-St	5.820 ± 0.185	1.780 ± 0.412
35	200	6Nb	1.261	0.894 ± 0.047	6Nb-St	9.620 ± 0.265	1.050 ± 0.745

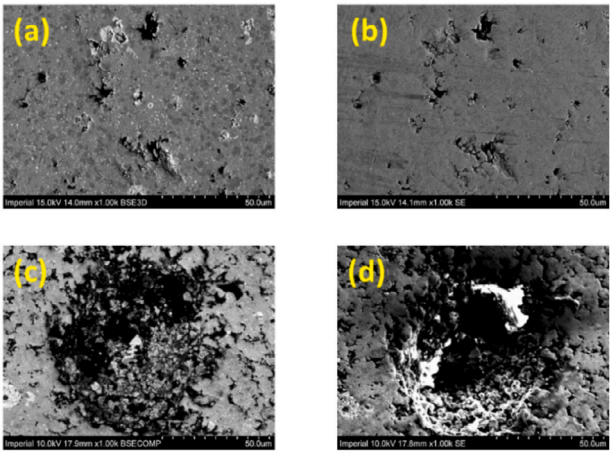

Fig. 19. Pits and crevices observed on clean surface of RR2450 ball.

glaze layers reduced wear through the repetitive removal of the formed corrosion films.

The microstructural investigation of the RR2450 alloy showed the formation of voids which can be reduced by a robust HIP process. The presence of hard silicide phases has a detrimental effect on the wear resistance of the counterface. Thus, there is an opportunity to improve the manufacturing process of RR2450 alloy and re-evaluate the alloy with optimised elemental composition. Upscaling the manufacturing process of these alloys can be challenging until the required quality control are in place.

The possibility for increasing the wear resistance of Fe-based hardfacing alloy without significantly reducing corrosion resistance has been demonstrated by alloying with nitrogen (>0.2 wt%) in Nitronic 60 and Nitromaxx. Pickering [63] showed a stronger reduction of SFE can be achieved by adding nitrogen. Additional benefits of high homogeneously distributed nitrogen content can increase solution strengthening and nitride formation.

Traditionally, carbides have been the focus for improving the wear resistance of hardfacing alloys. The presence of carbides, along with the silicides and nitrides, have strengthened Fe-based hardfacing alloys. Further study is required to quantify the effect of each of the hard phases. The hardness, wear resistance and toughness of these phases can be measured and used to determine the optimum ratio of these phases to get the ideal toughness vs. hardness ratio. This would require significant material characterisations and wear tests. An alternative would be to use the simulation techniques to determine the optimum ratio of the phases. The ideal elemental composition of metallic alloys can be determined using various simulation techniques, such as molecular dynamics simulations, Monte Carlo simulations, and finite element analysis [64–66]. These simulations can shed light on how alloys behave at the atomic and molecular levels by considering elements like crystal structure, flaws, and microstructure. Generally, simulations are an effective technique for designing and optimising metallic alloys and can accelerate the development of novel materials with enhanced properties.

The most significant discrepancies in volume losses between the repeats were in Cases 5Na and 5Nb (N-35 N 100 °C). Volume losses of Case 5Na were 2.66 mm^3, 1.30 ± 0.29 mm^3 for the ball and disc, respectively. Meanwhile, a lower volume loss of 1.11 mm^3 was obtained for the ball and 0.97 ± 0.09 mm^3 was obtained for the disc in Case 5Nb. Investigation of the ball surfaces revealed defects during ball manufacturing process. Fig. 19 shows SEM images of an area of the RR2450 ball with pits and crevices. Fig. 19a and b show BSE and SE images of 10 μm–20 μm pits. Meanwhile, Fig. 19c and d show BSE and SE images of bigger crevices of over 50 μm. These features were observed frequently at multiple random locations on the ball surfaces. The dispersion of these pits was not even or uniform and could have contributed to the lack of repeatability seen in all tests. These sliding tests are the first ever to be conducted using RR2450 alloy and the first attempt at converting RR2450 powder alloys into balls. Reduction in powder particle sizes and better surface finish will remove the surface defects observed, thus improving the sliding wear resistance. Following these tests, another batch of RR2450 balls was prepared for further sliding tests. The improvement in the manufacturing process meant the number of the pits were significantly reduced. Averaged surface

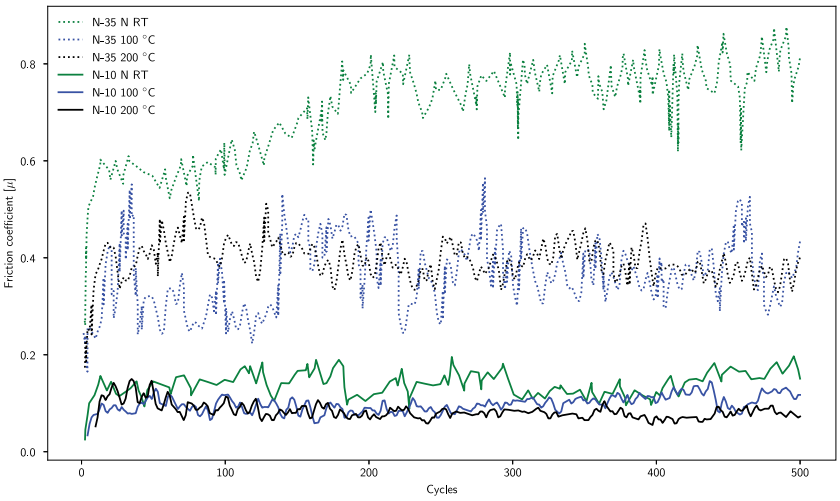

Fig. 20. Friction comparison of tests performed for Cases 1Na through to 6Na.

roughness was also reduced to Ra = 0.2 μm and Rq = 0.04 μm. Porosity was also reduced but to a lesser extent. Further improvement in the manufacturing process is needed to reduce porosity.

A torque meter recorded torque throughout the RR2450 vs. Haynes 25 sliding wear tests. The torque values were then converted to friction coefficients. Fig. 20 shows the relationship between load, temperature and friction. Only the first repeats of each test case are plotted here. As expected, the wear coefficients increased with the increased normal loads. The coefficient of friction measured for the first 500 cycles of sliding at room temperature was higher than at 100 °C and 200 °C tests for both loading conditions. Significant variations in friction coefficients were observed during the transition from the early running-in phase to a stabilised phase. This transition typically occurred within the first 200 cycles.

The second objective of this paper was to show the validity of the FEA models when non-uniform wear profiles were observed in the tests. The current FEA results are based on homogeneous materials, which is a simplification in the absence of detailed microstructural properties. The presented method cannot capture the significant variation of disc wear track profiles. Nonetheless, the presented method predicted the nominal wear profile. The non-uniformity of the wear track is governed by micro-level asperities, localised roughness, localised harder phases and localised tribologically transformed regions. The FEA method used here can be refined by considering localised variations by adjusting the hardness of the localised areas and introducing asperities in the model.

The study of local surface tribochemistry will show the chemical reactions that occurs at the contact surfaces and the effect on wear, friction, frictional heat and corrosion properties locally. The current tribometer instrumentation is not able to capture local surface tribochemistry. So future studies can account for tribochemistry that can show how new compounds and tribofilms are generated and their effect on wear. This can be also incorporated in the FEA results by changing the surface properties, such as local friction coefficient and material hardness. These changes can also be potentially coupled to changes in the surface topography, which results in localised stress concentrations and reduction of contact area between the surfaces. This in turn can be linked to an increase friction and thus more wear.

Broadly speaking, change in material properties at the tribologically transformed region will change the local stiffness and strength, change thermal conductivity of materials, and change the corrosion resistance of the materials. Simulation studies focusing on tribochemistry (and/or mechanochemistry) and wear have recently provided a relatively new area of study, which is receiving increasing attention given the improvement of modelling tools and resources to include different chemical, physical and mechanical effects as well as linking simulations across the scales. Semi-deterministic tribochemical models can be developed at the required length scale as for example done to study both topographical variations and tribochemical evolutions by some researchers [67–69], while mechanochemical reactions can also be captured using molecular dynamics simulations, as suggested by Vakis et al. [70]; this has recently led to workflows that can provide very useful information about the evolution of the surfaces for many different compounds and surfaces, which are very rich phenomena [71–73], and can also be directly linked to film formation at the larger scales via recently developed mesoscale bridging methods [74].

Since FEA is a versatile tool, the developed method is applicable to a wide range of sliding wear tests. Changes in local surface topography can be modelled in FEA using subroutines such as UMESHMOTION and FRIC. To enhance the model further, the variation of material properties at tribologically transferred regions can also be modelled in FEA using subroutines such as UMAT to define the mechanical constitutive behaviour of a material and its evolution at an elemental level.

6. Concluding remarks

The excellent wear and corrosion resistance of Co-based alloys make them desirable for tribological applications in the nuclear industry. However, neutron activation of the Co-based alloys leads to significant occupational radiation doses. An alternative Fe-based alloy called RR2450 was developed by Rolls-Royce plc to replace Co-based alloys. This is the first comprehensive study evaluating the sliding wear resistance of RR2450 in the representative PWR conditions.

RR2450 is a highly alloyed derivative of Tristelle 5183, a Fe-based stainless steel alloy. Duplex austenitic and ferritic phases are present in RR2450. It also contains a high fraction of carbides and hard silicide phases. The sliding counterface of RR2450 balls was Haynes 25 discs. Haynes 25 is a Co-based alloy commonly used for rolling and raceway components of rolling element bearings. A total of 16 sliding tests were conducted using two tribometers at two labs. Four tests were carried out at Imperial College London at ambient temperature and at 80 °C. The remaining twelve tests were performed at ambient temperature, 100 °C and 200 °C in an autoclave at the University of Nottingham. The total volume loss of the disc ranged between 4 times and 8 times higher than the volume loss of balls for 10 N load and lower temperature cases. However, at the higher load of 35 N and higher temperatures of 100 °C and 200 °C, significant wear loss is observed on the balls. Meanwhile, there was no significant change in the volume loss of the disc counterfaces at these high-temperature high-load cases. The wear performance of the RR2450 balls degraded at higher loads and

temperatures. Ball's volume loss for the Tests 3Na, 3Nb (N-10 N 200 °C) is around double when compared with Tests 2Na, 2Nb (N-10 N 100 °C) and Tests 4Na, 4Nb (N-35 N RT). The variation of disc wear volumes for all three cases is significantly less. This shows temperature plays an important role in the degradation of wear resistance properties of RR2450 balls.

Among these tests, two wear tests with uneven wear tracks at two normal load cases were selected for detailed 3D finite element analysis. Cases 2Na (N-10 N 100 °C) and 5Na (N-35 N 100 °C) had the highest variations on wear track dimensions. A previously developed FEA method appropriate for 3D surfaces was used where contact pressures are calculated on both surfaces. In the absence of localised wear rates, averaged wear rates of the ball and disc surfaces from the tests were used to generate representative wear profiles of the ball and disc surfaces. The maximum deviations from the mean wear profiles were for Case 5Na. While current FEA results are based on homogeneous materials and cannot capture significant variations in wear track profiles, the method presented was able to predict nominal wear profile. Non-uniformity of wear tracks is influenced by micro-level asperities, localised roughness, and tribologically transformed regions. To improve FEA models, hardness of localised areas can be adjusted and asperities can be introduced.

The microstructural investigation of the RR2450 alloy showed the formation of voids that become pits and crevices on the surface. The voids and the presence of hard silicide phases have a detrimental effect on the wear resistance of the counterface. A comparison with like-for-like tests results with a Co-based alloy, Stellite 20, was carried out. The comparison showed RR2450 demonstrates similar wear resistance to Co-based alloys at nuclear reactor conditions.

CRediT authorship contribution statement

Ajit Bastola: Wear characterisation and measurements, Microscopy, Finite element studies, Write up. **Ruby McCarron:** Sliding tests, Microscopy and Write up. **Philip Shipway:** Resources, Facilities, Review and approval. **David Stewart:** Review and approval. **Daniele Dini:** Research idea, Supervision, Review, Verification and approval.

Declaration of competing interest

The authors declare that they have no known competing financial interests or personal relationships that could have appeared to influence the work reported in this paper.

Data availability

Data will be made available on request.

Acknowledgements

The authors thank Professor Philip Shipway's team for performing sliding tests at the University of Nottingham. All authors approved the version of the manuscript to be published.

Appendix A. Supplementary information

Supplementary material related to this article can be found online at https://doi.org/10.1016/j.wear.2023.205186.

References

[1] Nuclear Energy Agency, OECD, Occupational exposures at nuclear power plants, twenty-seventh annual report of the ISOE programme, 2017, 2020, URL: http://www.isoe-network.net/publications/pub-resources/isoe-annual-reports/4331-isoe-annual-report-2017/file.html.

[2] J. Guidez, A. Saturnin, Evolution of the collective radiation dose of nuclear reactors from the 2nd through to the 3rd generation and 4th generation sodium-cooled fast reactors, EPJ Nucl. Sci. Technol. 3 (2017) 32, http://dx.doi.org/10.1051/epjn/2017024.

[3] Geir Meyer, Egil Stokke, Description of Sizewell B Nuclear Power Plant, Institutt for energiteknikk (IFE), Halden, 1997, URL: https://inis.iaea.org/collection/NCLCollectionStore/{_}Public/29/010/29010110.pdf.

[4] I. Toshihisa, I. Shou, Y. Tsutomu, N. Hiroshi, I. Yuichi, Development of in-vessel type control rod drive mechanism for marine reactor, J. Nucl. Sci. Technol. 38 (7) (2001) 557–570, http://dx.doi.org/10.1080/18811248.2001.9715067.

[5] L. Cachon, J. Denape, F. Sudreau, L. Lelait, Tribological qualification of cobalt-free coatings for pressurized water reactor primary-circuit gate valve applications, Surf. Coat. Technol. 85 (3) (1996) 163–169, http://dx.doi.org/10.1016/0257-8972(95)02672-X.

[6] B. Cockeram, Development of wear-resistant coatings for cobalt–base alloys, Surf. Coat. Technol. 120–121 (1999) 509–518, http://dx.doi.org/10.1016/S0257-8972(99)00492-2.

[7] H. Ocken, Reducing the cobalt inventory in light water reactors, Nucl. Technol. 68 (1) (1985) 18–28, http://dx.doi.org/10.13182/NT85-A33563.

[8] W.B. Burdett, Development of cobalt free wear resistant alloys for nuclear applications, Surf. Eng. 8 (2) (1992) 131–135, http://dx.doi.org/10.1179/sur.1992.8.2.131.

[9] C.B. Bahn, B.C. Han, J.S. Bum, I.S. Hwang, C.B. Lee, Wear performance and activity reduction effect of Co-free valves in PWR environment, Nucl. Eng. Des. 231 (1) (2004) 51–65, http://dx.doi.org/10.1016/j.nucengdes.2004.02.001.

[10] K.Y. Lee, G.G. Kim, J.H. Kim, S.H. Lee, S.J. Kim, Sliding wear behavior of hardfacing alloys in a pressurized water environment, Wear 262 (7–8) (2007) 845–849, http://dx.doi.org/10.1016/j.wear.2006.08.015.

[11] A. Pauschitz, M. Roy, F. Franek, Mechanisms of sliding wear of metals and alloys at elevated temperatures, Tribol. Int. 41 (7) (2008) 584–602, http://dx.doi.org/10.1016/j.triboint.2007.10.003, URL: http://linkinghub.elsevier.com/retrieve/pii/S0301679X07001715.

[12] D. Bowden, D. Stewart, M. Preuss, The identification of a silicide phase and its crystallographic orientation to ferrite within a complex stainless steel, J. Nucl. Mater. 517 (2019) 356–361, http://dx.doi.org/10.1016/j.jnucmat.2019.02.028.

[13] J. Vikström, Galling resistance of hardfacing alloys replacing stellite, Wear 179 (1–2) (1994) 143–146, http://dx.doi.org/10.1016/0043-1648(94)90232-1.

[14] M. Roy, A. Pauschitz, J. Wernisch, F. Franek, Effect of mating surface on the high temperature wear of 253 MA alloy, Mater. Corros. 55 (4) (2004) 259–273, http://dx.doi.org/10.1002/maco.200303715.

[15] I. Inman, P. Datta, H. Du, J. Burnell-Gray, S. Pierzgalski, Q. Luo, Studies of high temperature sliding wear of metallic dissimilar interfaces, Tribol. Int. 38 (9) (2005) 812–823, http://dx.doi.org/10.1016/j.triboint.2005.02.007, URL: http://www.sciencedirect.com/science/article/pii/S0301679X05000794. Special Issue in Memory of Professor Tony Ball.

[16] A. Pauschitz, M. Roy, F. Franek, On the chemical composition of the layers formed during sliding of metallic alloys at high temperature, Tribologia nr 2 (2003) 127–143.

[17] S.J. Kim, J.K. Kim, Effects of temperature and contact stress on the sliding wear of Ni-base deloro 50 hardfacing alloy, J. Nucl. Mater. 288 (2–3) (2001) 163–169, http://dx.doi.org/10.1016/S0022-3115(00)00711-X.

[18] H. Ocken, The galling wear resistance of new iron-base hardfacing alloys: a comparison with established cobalt- and nickel-base alloys, Surf. Coat. Technol. 76–77 (PART 2) (1995) 456–461, http://dx.doi.org/10.1016/0257-8972(95)02573-1.

[19] S. Atamert, D.H.K.D.H. Bhadeshia, Stability, Wear Resistance, and Microstructure of Iron, Cobalt and Nickel-Based Hardfacing Alloys (Ph.D. thesis), 1988, http://dx.doi.org/10.17863/CAM.14238.

[20] D. Bowden, Y. Krysiak, L. Palatinus, D. Tsivoulas, S. Plana-Ruiz, E. Sarakinou, U. Kolb, D. Stewart, M. Preuss, A high-strength silicide phase in a stainless steel alloy designed for wear-resistant applications, Nature Commun. 9 (1) (2018) 1–10, http://dx.doi.org/10.1038/s41467-018-03875-9.

[21] M.J. Carrington, J. Daure, V.L. Ratia, P.H. Shipway, D.G. McCartney, D.A. Stewart, Microstructural characterisation of tristelle 5183 (Fe-21%Cr-10%Ni-7.5%Nb-5%Si-2%C in wt%) alloy powder produced by gas atomisation, Mater. Des. 164 (2019) 107548, http://dx.doi.org/10.1016/j.matdes.2018.107548.

[22] J.K. Kim, S.J. Kim, The temperature dependence of the wear resistance of iron-base NOREM 02 hardfacing alloy, Wear 237 (2) (2000) 217–222, http://dx.doi.org/10.1016/S0043-1648(99)00326-9.

[23] P. Crook, I. Kokomo, R.D. Zordan, N. Raleigh, Nuclear grade steels, 1987, URL: https://patentimages.storage.googleapis.com/9d/22/6f/84333728858f54/US4643767.pdf.

[24] R. Smith, M. Doran, D. Gandy, S. Babu, L. Wu, A.J. Ramirez, P.M. Anderson, Development of a gall-resistant stainless-steel hardfacing alloy, Mater. Des. 143 (2018) 38–48, http://dx.doi.org/10.1016/j.matdes.2018.01.020.

[25] C. Zhao, D. Stewart, J. Jiang, F.P. Dunne, A comparative assessment of iron and cobalt-based hard-facing alloy deformation using HR-EBSD and HR-DIC, Acta Mater. 159 (2018) 173–186, http://dx.doi.org/10.1016/j.actamat.2018.08.021.

[26] D.H. Persson, S. Jacobson, S. Hogmark, Effect of temperature on friction and galling of laser processed norem 02 and stellite 21, Wear 255 (1–6) (2003) 498–503, http://dx.doi.org/10.1016/S0043-1648(03)00122-4.

[27] J. Sulley, D. Stewart, HIPed Hard Facings for Nuclear Applications: Materials, Key Potential Defects and Mitigating Quality Control Measures, Technical Report, 2016, URL: http://asmedigitalcollection.asme.org/ICONE/proceedings-pdf/ICONE24/50015/V001T03A034/2452653/v001t03a034-icone24-61106.pdf.

[28] W. Burdett, Stainless steel alloy patent, 1997, URL: https://patentimages.storage.googleapis.com/5b/65/d8/238c8bc606c0a3/US5660939.pdf.

[29] B.V. Cockeram, Corrosion Resistance and Electrochemical Potentiokinetic Reactivation Testing Of Some Iron-base Hardfacing Alloys, Technical Report, Bettis Atomic Power Laboratory, West Mifflin, 1999, URL: https://inis.iaea.org/collection/NCLCollectionStore/_Public/31/051/31051160.pdf.

[30] F.G. Wasserman, S.S.M. Tavares, J.M. Pardal, F.B. Mainier, R.A. Faria, C.d.S. Nunes, Effects of low temperature aging on the mechanical properties and corrosion resistance of duplex and lean duplex stainless steels UNS S32205 and UNS S32304, Rem: Rev. Escola Minas 66 (2) (2013) 193–200.

[31] H. Beattie, F. VerSnyder, Microconstituents in high temperature alloys, Trans. Amer. Soc. Metals 45 (1953) 397–428, http://dx.doi.org/10.1590/S0370-44672013000200009.

[32] S. Wlodek, Embrittlement of a Co-Cr-W (L-605) alloy, Trans. ASM 56 (3) (1963) 287–303.

[33] N. Yukawa, K. Sato, Proc. Int. Conf. on strength of metals and alloys I (ICSMA I), 1967.

[34] D.L. Klarstrom, Wrought cobalt-base superalloys, J. Mater. Eng. Perform. 2 (1993) 523–530, https://doi.org/10.1007/BF02661736.

[35] L. García Fresnillo, A. Chyrkin, T. Hüttel, C. Böhme, J. Barnikel, D. Grüner, F. Schmitz, W.J. Quadakkers, Oxide scale formation and subsurface phase transformations during long-term steam exposure of the cobalt base alloy 25, Mater. Corros. 63 (10) (2012) 878–888, http://dx.doi.org/10.1002/MACO.201206683, https://doi.org/10.1002/MACO.201206683.

[36] W. Conshohocken, ASTM G40-17 standard terminology relating to wear and erosion, 2017, pp. 1–9, http://dx.doi.org/10.1520/G0040-17.

[37] H.C. Meng, K.C. Ludema, Wear models and predictive equations: their form and content, Wear 181–183 (PART 2) (1995) 443–457, http://dx.doi.org/10.1016/0043-1648(95)90158-2.

[38] ASTM International, G99 – 17: Standard test method for wear testing with a pin-on-disk apparatus , 2017, pp. 1–6, http://dx.doi.org/10.1520/G0099-17.

[39] J.F. Archard, W. Hirst, The wear of metals under unlubricated conditions, Proc. R. Soc. Lond. Ser. A: Math. Phys. Eng. Sci. 236 (1206) (1956) 397–410, http://dx.doi.org/10.1098/rspa.1956.0144.

[40] J.F. Molinari, M. Ortiz, R. Radovitzky, E.A. Repetto, Finite-element modeling of dry sliding wear in metals, Eng. Comput. (Swansea, Wales) 18 (3–4) (2001) 592–609, http://dx.doi.org/10.1108/00368790110407257.

[41] V. Hegadekatte, N. Huber, O. Kraft, Finite element based simulation of dry sliding wear, Modelling Simul. Mater. Sci. Eng. 13 (1) (2005) 58–59, http://dx.doi.org/10.1088/0965-0393/13/1/005.

[42] P. Põdra, S. Andersson, Simulating sliding wear with finite element method, Tribol. Int. 32 (2) (1999) 71–81, http://dx.doi.org/10.1016/S0301-679X(99)00012-2.

[43] A. Söderberg, S. Andersson, Simulation of wear and contact pressure distribution at the pad-to-rotor interface in a disc brake using general purpose finite element analysis software, Wear 267 (12) (2009) 2243–2251, http://dx.doi.org/10.1016/j.wear.2009.09.004.

[44] E.M. Bortoleto, A.C. Rovani, V. Seriacopi, F.J. Profito, D.C. Zachariadis, I.F. Machado, A. Sinatora, R.M. Souza, Experimental and numerical analysis of dry contact in the pin on disc test, Wear 301 (1–2) (2013) 19–26, http://dx.doi.org/10.1016/j.wear.2012.12.005.

[45] A. Bastola, D. Stewart, D. Dini, Three-dimensional finite element simulation and experimental validation of sliding wear, Wear 504–505 (2022) 204402, http://dx.doi.org/10.1016/J.WEAR.2022.204402.

[46] L. Johansson, Model and numerical algorithm for sliding contact between two elastic half-planes with frictional heat generation and wear, Wear 160 (1) (1993) 77–93, http://dx.doi.org/10.1016/0043-1648(93)90408-E.

[47] L. Gallego, D. Nélias, C. Jacq, A comprehensive method to predict wear and to define the optimum geometry of fretting surfaces, J. Tribol. 128 (3) (2006) 476, http://dx.doi.org/10.1115/1.2194917.

[48] V. Hegadekatte, S. Kurzenhäuser, N. Huber, O. Kraft, A predictive modeling scheme for wear in tribometers, Tribol. Int. 41 (11) (2008) 1020–1031, http://dx.doi.org/10.1016/j.triboint.2008.02.020.

[49] Haynes International, HAYNES® 25 alloy Principle Features, Technical Report, 2022, pp. 1–2, URL: https://haynesintl.com/docs/default-source/pdfs/new-alloy-brochures/high-temperature-alloys/brochures/25-brochure.pdf.

[50] N.L. Loh, K.Y. Sia, An overview of hot isostatic pressing, J. Mater Process. Technol. 30 (1) (1992) 45–65, http://dx.doi.org/10.1016/0924-0136(92)90038-T.

[51] D. Klarstrom, Heat treatment of cobalt-base alloys, in: Heat Treating of Nonferrous Alloys, ASM International, 2016, http://dx.doi.org/10.31399/asm.hb.v04e.a0006267.

[52] I.A. Inman, Compacted Oxide Layer Formation Under Conditions of Limited Debris Retention At the Wear Interface During High Temperature Sliding Wear of Superalloys (Ph.D. thesis), Northumbria University, 2003, p. 369.

[53] Y.-H. Zhou, M.G. Harmelin, J.-Y. Bigot, Sintering behaviour of ultra-fine Fe, Ni and Fe-25wt%Ni powders, Scr. Metall. 23 (1989) 1391–1396.

[54] F.H. Stott, High-temperature sliding wear of metals, Tribol. Int. 35 (2002) 489–495.

[55] I.A. Inman, P. Datta, Studies of high temperature sliding wear of metallic dissimilar interfaces IV: Nimonic 80A versus incoloy 800HT, Tribol. Int. 44 (2011) 1902–1919.

[56] A. Dréano, S. Fouvry, G. Guillonneau, A tribo-oxidation abrasive wear model to quantify the wear rate of a cobalt-based alloy subjected to fretting in low-to-medium temperature conditions, Tribol. Int. 125 (May) (2018) 128–140, http://dx.doi.org/10.1016/j.triboint.2018.04.032.

[57] K. Luo, S. Li, G. Xu, S.R.E. Hosseini, J. Lu, Hot corrosion behaviors of directed energy deposited inconel 718/haynes 25 functionally graded material at 700 °c and 900 °c, Corros. Sci. 197 (2022) 110040, http://dx.doi.org/10.1016/j.corsci.2021.110040.

[58] I. McColl, J. Ding, S. Leen, Finite element simulation and experimental validation of fretting wear, Wear 256 (11–12) (2004) 1114–1127, http://dx.doi.org/10.1016/J.WEAR.2003.07.001.

[59] R. McCarron, D. Stewart, P. Shipway, D. Dini, Sliding wear analysis of cobalt based alloys in nuclear reactor conditions, Wear 376–377 (2017) 1489–1501, http://dx.doi.org/10.1016/j.wear.2016.12.018.

[60] E. Lemaire, M. Le Calvar, Evidence of tribocorrosion wear in pressurized water reactors, Wear 249 (5–6) (2001) 338–344, http://dx.doi.org/10.1016/S0043-1648(00)00544-5.

[61] V.L. Ratia, D. Zhang, M.J. Carrington, J.L. Daure, D.G. McCartney, P.H. Shipway, D.A. Stewart, Comparison of the sliding wear behaviour of self-mated hiped stellite 3 and stellite 6 in a simulated PWR water environment, Wear 426–427 (January) (2019) 1222–1232, http://dx.doi.org/10.1016/j.wear.2019.01.116.

[62] R.J. Wood, Marine wear and tribocorrosion, Wear 376–377 (2017) 893–910, http://dx.doi.org/10.1016/j.wear.2017.01.076.

[63] F. Pickering, Proc. of the conf. on stainless steels, band 320, 1984, p. 2.

[64] M. Beyramali Kivy, Y. Hong, M. Asle Zaeem, A review of multi-scale computational modeling tools for predicting structures and properties of multi-principal element alloys, Metals 9 (2) (2019) 254, https://doi.org/10.3390/met9020254.

[65] S.J. Eder, M. Rodríguez Ripoll, U. Cihak-Bayr, D. Dini, C. Gachot, Unraveling and mapping the mechanisms for near-surface microstructure evolution in CuNi alloys under sliding, ACS Appl. Mater. Interfaces 12 (28) (2020) 32197–32208, http://dx.doi.org/10.1021/acsami.0c09302.

[66] S.J. Eder, P.G. Grützmacher, M.R. Ripoll, C. Gachot, D. Dini, Does speed kill or make friction better?—Designing materials for high velocity sliding, Appl. Mater. Today 29 (2022) 101588, https://doi.org/10.1016/j.apmt.2022.101588.

[67] A. Azam, A. Ghanbarzadeh, A. Neville, A. Morina, M.C. Wilson, Modelling tribochemistry in the mixed lubrication regime, Tribol. Int. 132 (2019) 265–274, http://dx.doi.org/10.1016/j.triboint.2018.12.024.

[68] Z. Chen, C. Gu, T. Tian, Modeling of formation and removal of ZDDP tribofilm on rough surfaces, Tribol. Lett. 69 (2021) 1–9, URL: https://doi.org/10.1007/s11249-020-01393-8.

[69] A. Ghanbarzadeh, E. Piras, I. Nedelcu, V. Brizmer, M.C. Wilson, A. Morina, D. Dowson, A. Neville, Zinc dialkyl dithiophosphate antiwear tribofilm and its effect on the topography evolution of surfaces: A numerical and experimental study, Wear 362–363 (2016) 186–198, http://dx.doi.org/10.1016/j.wear.2016.06.004.

[70] A. Vakis, V. Yastrebov, J. Scheibert, L. Nicola, D. Dini, C. Minfray, A. Almqvist, M. Paggi, S. Lee, G. Limbert, J. Molinari, G. Anciaux, R. Aghababaei, S. Echeverri Restrepo, A. Papangelo, A. Cammarata, P. Nicolini, C. Putignano, G. Carbone, S. Stupkiewicz, J. Lengiewicz, G. Costagliola, F. Bosia, R. Guarino, N. Pugno, M. Müser, M. Ciavarella, Modeling and simulation in tribology across scales: An overview, Tribol. Int. 125 (2018) 169–199, http://dx.doi.org/10.1016/j.triboint.2018.02.005.

[71] C. Ayestarán Latorre, J.E. Remias, J.D. Moore, H.A. Spikes, D. Dini, J.P. Ewen, Mechanochemistry of phosphate esters confined between sliding iron surfaces, Commun. Chem. 4 (1) (2021) 178, URL: https://www.nature.com/articles/s42004-021-00615-x.

[72] A. Martini, S.J. Eder, N. Dörr, Tribochemistry: a review of reactive molecular dynamics simulations, Lubricants 8 (4) (2020) 44, URL: https://doi.org/10.3390/lubricants8040044.

[73] Z. Li, I. Szlufarska, Physical origin of the mechanochemical coupling at interfaces, Phys. Rev. Lett. 126 (2021) 076001, http://dx.doi.org/10.1103/PhysRevLett.126.076001.

[74] S. Ntioudis, J.P. Ewen, D. Dini, C.H. Turner, A hybrid off-lattice kinetic Monte Carlo/molecular dynamics method for amorphous thin film growth, Comput. Mater. Sci. 229 (2023) 112421, URL: https://doi.org/10.1016/j.commatsci.2023.112421.